

**INVESTIGATION OF THERMOACOUSTIC
PERFORMANCE OF STANDING AND
TRAVELING WAVE THERMOACOUSTIC
ENGINES**

by

Konstantin N. Tourkov

B.S. in Mechanical Engineering, University of Pittsburgh, 2011

Submitted to the Graduate Faculty of
the Swanson School of Engineering in partial fulfillment
of the requirements for the degree of
Master of Science in Mechanical Engineering

University of Pittsburgh

2013

UNIVERSITY OF PITTSBURGH
SWANSON SCHOOL OF ENGINEERING

This thesis was presented

by

Konstantin N. Tourkov

It was defended on

March 26, 2013

and approved by

Laura A. Schaefer, Ph.D., Associate Professor,

Department of Mechanical Engineering and Materials Science

Jeffrey S. Vipperman, Ph.D., Associate Professor,

Department of Mechanical Engineering and Materials Science

Mark Kimber, Ph.D., Assistant Professor,

Department of Mechanical Engineering and Materials Science

Thesis Advisor: Laura A. Schaefer, Ph.D., Associate Professor,

Department of Mechanical Engineering and Materials Science

INVESTIGATION OF THERMOACOUSTIC PERFORMANCE OF STANDING AND TRAVELING WAVE THERMOACOUSTIC ENGINES

Konstantin N. Tourkov, M.S.

University of Pittsburgh, 2013

A standing wave thermoacoustic engine was designed and constructed to examine the effect of curvature on thermoacoustic performance. Sound pressure level at the pressure node of the engine was recorded in conjunction with the temperature at the hot and ambient sides of the stack. Curvature was varied using flexible tubing from 0° to 45° . It was found that the curvature had a negative effect on the thermoacoustic intensity, measured using the sound pressure level and the temperature difference between the hot and ambient sides of the stack. Additionally, a strong relationship between the sound pressure level and the temperature behavior was identified. The findings of the investigation were applied to a study of a traveling wave engine. A looped tube design was employed with a regenerator mounted in a straight section of the tube. Thermocouples were mounted in the regenerator to investigate the temperature behavior. Initial results of the thermoacoustic effect were established by calculating the difference in behavior between operation with oscillation and without. These were followed by an investigation of the relationship between the temperature behavior and the positioning of the regenerator in the looped tube. An optimal spacing was identified for positioning the stack in the straight portion of the tube.

TABLE OF CONTENTS

1.0 INTRODUCTION	1
1.1 Brief History	1
1.2 Thermoacoustic Engines: Standing Wave and Traveling Wave	2
1.2.1 Standing Wave Engines	3
1.2.2 Traveling Wave Engines	4
1.3 Motivation for Thermoacoustic Refrigeration	8
1.3.1 Absorption Cycles	8
1.3.2 Vapor Compression	10
1.3.3 Thermoacoustic Cooling	11
1.4 Goals of This Work	12
2.0 THERMOACOUSTIC THEORY	13
2.1 Linear Acoustic Theory	13
2.2 Streaming Losses	16
2.2.1 Gedeon Streaming	16
2.2.2 Rayleigh Streaming	18
2.3 Acoustic Losses	20
2.4 Viscous Losses	21
2.5 Thermal Losses	22
3.0 STANDING WAVE INVESTIGATION	26
3.1 Design and Construction	26
3.1.1 Stack Length and Position	26
3.1.2 Pore Geometry and Size	27

3.1.3 Resonator	27
3.1.4 Data Acquisition	28
3.2 Results: Temperature Behavior	30
3.2.1 Hot Side Behavior	30
3.2.2 Ambient Side Behavior	33
3.2.3 Trends Between Temperature and Curvature	34
3.3 Results: Acoustic Behavior	36
3.3.1 General Oscillation Behavior	36
3.3.2 Trends Between SPL and Curvature	36
4.0 TRAVELING WAVE INVESTIGATION	40
4.1 Design and Construction	40
4.1.1 Resonator	40
4.1.2 Regenerator	41
4.2 Experimental Setup	43
4.3 Results: Stack Positioning Effects on Thermoacoustic Behavior	45
4.3.1 Patterns In Thermoacoustic Behavior	45
4.3.2 Ambient Side Behavior	48
4.3.3 Hot Side Behavior	48
4.3.4 Stack Placement and Intensity of The Thermoacoustic Effect	49
4.4 Discussion	51
5.0 CONCLUSIONS AND FURTHER RECOMMENDATIONS	53
5.1 Conclusions	53
5.2 Future Work	54
BIBLIOGRAPHY	55

LIST OF FIGURES

1	Quarter-wave standing wave TAE [11]	3
2	Standing wave TAE cycle	5
3	Standing wave TAE P-V diagram corresponding to cycle shown in Figure 2.	5
4	Various traveling wave engine designs [18]	6
5	Diagram of a traveling wave cycle	7
6	Traveling wave TAE P-V diagram corresponding to cycle in Figure 5 [18].	8
7	Diagram of a typical absorption cycle	9
8	Diagram of a typical VC cycle	10
9	Illustration of net mass flow occurrence in pulse tube [33].	18
10	Mass flux profile in pulse tubes from central axis to wall [33].	18
11	Image of streaming taken using Doppler velocimetry [38].	19
12	Velocity field observed using LDA and BSA [39].	19
13	Relation between axial acoustic and axial streaming velocities [39].	19
14	Real and imaginary parts of $F(\lambda)$ for various pore geometries [28].	20
15	Experimental results compared to analytical forms for heat compared to the temperature difference [40].	21
16	TAR design [45]	23
17	Thermoacoustic refrigerator thermal and viscous losses [45].	23
18	TAR hot side exchanger thermal and viscous losses [45].	24
19	TAR hot side exchanger thermal and viscous losses [32].	24
20	Convective losses [32]	25
21	Radiation losses [32]	25

22	Diagram of standing wave device used in testing	28
23	Diagram of hot side of stack assembly	29
24	Initial response of SWTAE to 5V input	30
25	Hot and ambient side temperature and SPL results for each of 3 runs for all curvatures	31
26	Hot side average histogram for each curvature.	32
27	Hot side averages for each curvature	32
28	Ambient side average histogram for each curvature.	33
29	Ambient side averages for each curvature	34
30	Hot side overall averages with linear regression prediction.	35
31	Ambient side overall averages.	35
32	Sound Pressure Histogram	37
33	Average SPL for each curvature.	38
34	Average SPL with regression analysis.	38
35	Sound Pressure vs. Temperature Difference	39
36	Picture of traveling wave TAE	42
37	Housing design used to insure air tightness.	42
38	Regenerator used in the construction of the TAE.	42
39	Ambient side thermocouple positioning	44
40	Regenerator position diagram	44
41	Hot side individual runs.	46
42	Ambient side individual runs.	46
43	Hot side thermocouple readings.	46
44	Ambient side thermocouple readings.	46
45	Hot side temperature difference	47
46	Variation in hot side calculation.	47
47	Percent error with respect to lower hot side average	47
48	Ambient side averaged oscillation and no oscillation runs.	48
49	Ambient side temperature difference between run averages.	48
50	Hot side averaged oscillation and no oscillation runs.	49

51	Hot side temperature difference between run averages.	49
52	Normalized ambient temperature difference.	50
53	Normalized hot temperature difference.	50
54	Ambient side stack temperature vs. stack positioning.	51
55	Hot side stack temperature vs. stack positioning.	51
56	Temperature difference across regenerator	52
57	Hot side stack temperature vs. stack positioning.	52

1.0 INTRODUCTION

Thermoacoustics is concerned with the study of the relationship between thermal gradients and acoustic vibrations. As a general field, it has been around for some time, but has only recently made great strides in developing devices employing this phenomenon. While it covers a large host of applications, the most prominent that has been researched is the use of thermoacoustics in heat pumping and refrigeration. Due to their simplicity and low environmental impact, thermoacoustic refrigerators (TARs) are well suited to large scale applications and currently can be found in the field of cryogenic cooling, where traditional vapor compression systems experience difficulties.

1.1 BRIEF HISTORY

The study of the thermoacoustic effect began in 1777, when Byron Higgins experimented with a hydrogen flame to produce sound in a large open pipe [1, 2]. Much later, in 1859, Rijke recreated the Higgins experiment with a hot wire mesh replacing the hydrogen flame [3]. Around the same time, in 1850, Sondhauss experimented with applying heat to a pipe that had a closed end and an open end, producing sound, the frequency of which, Sondhauss concluded, had a dependency on the length of the tube [4]. The first quantitative analysis came from Kirchoff in 1868 with equations describing the effects of the thermal attenuation of sound [5]. Kirchoff based his analysis on the use of the Navier-Stokes equations and the Fourier Law of heat conduction to develop a model for the propagation of acoustic vibrations through a fluid in a tube with a wall held at constant temperature. His theory was later applied by Kramers in an attempt to describe the method by which a tube that is closed and

hot at one end and cold and open at the other produces acoustic vibrations [6]. Both assumed boundary layer behavior, implying that the tube is much wider than the wall frictional layer. However, both Kramers' and Kirchoff's predictions proved to present results that did not accurately match observations.

A more complete analysis came from Rott in 1969 with a general linear theory of thermoacoustics [7]. Rott's theory was based on an assumption that the tube radius is significantly smaller than its length. His theory, discussed in Chapter 2, proved successful in modeling thermoacoustic behavior and became a tool for the design of thermoacoustic engines and refrigerators. A decade later, Ceperley was the next person to make a significant contribution in his proposal of the traveling wave thermoacoustic engine [8]. Using a feedback inertance, Ceperley was able to tune the pressure and velocity fields to operate in phase, creating an acoustic Stirling engine. Ceperley's concept was tested by Yazaki et al. [9] in 1998, and later applied by Swift and Backhaus [10] in their design of a thermoacoustic Stirling heat engine (TASHE). Simultaneously, starting in the 1980s, the Los Alamos National Laboratory (LANL) has conducted research on thermoacoustic engines and refrigerators, resulting in significant contributions to improving the efficiency of thermoacoustic engines and COP for thermoacoustic refrigerators.

1.2 THERMOACOUSTIC ENGINES: STANDING WAVE AND TRAVELING WAVE

Standing wave and traveling wave engines operate under similar thermodynamic cycles. The traveling wave cycle is identical to the Stirling cycle, leading traveling wave engines to often be referred to as Stirling thermoacoustic engines. The standing wave cycle can best be described as a modified version of the Stirling cycle, since it has many similarities with the traveling wave cycle. The differences in the operation of the two cycles are further discussed below, illustrating the fundamental reason why traveling wave engines are inherently more efficient than their standing wave counterparts.

1.2.1 Standing Wave Engines

Quarter wavelength standing wave devices, particularly engines, are the simplest thermoacoustic devices to build and operate. They consist of a resonator that, as the name suggests, is the length of a quarter of the wavelength of the acoustic oscillation. The resonator is closed on one end and open on the other, as shown in Figure 1. A stack is placed near the closed end with two heat exchangers on each side, configured on the closed end to either input heat for an engine, or draw heat away for a refrigerator. The length of the resonator in relation to the wavelength causes the maximum pressure oscillation (antinode) to occur at the closed end and no pressure oscillation (node) to occur at the open end. The velocity behavior is shifted 90° from the pressure, with a node at the closed end, and an antinode at the open end.

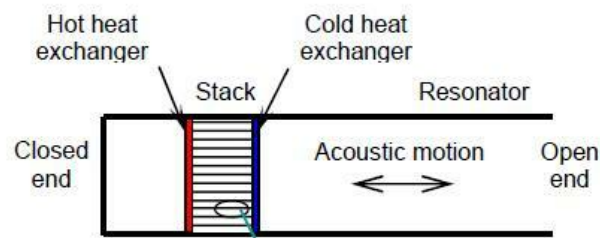


Figure 1: Quarter-wave standing wave TAE [11]

The standing wave cycle starts with the compression and movement of the gas towards a hot heat exchanger. This part of the cycle is nearly adiabatic as the time it takes for the gas to travel and the surface area of the pores facilitate very little movement of heat. In the second step, the gas is heated by the stack walls, while simultaneously undergoing expansion. It then moves toward the cold side heat exchanger, expanding along the way. This step of the process, like the first, is adiabatic. The gas arrives at the cold heat exchanger at an elevated temperature, and is thus cooled, while contracting, completing the cycle [12]. Figure 2 demonstrates the steps of the cycle while Figure 3 shows the steps on a pressure-volume diagram.

The cycle described above operates on the requirement of adiabatic movement in the first and third steps. This is due to the out of phase pressure and velocity behavior of the standing

wave engine. It is necessary that the thermal expansion occurs at the highest pressure to generate more work than is required to compress the gas for the extraction of heat at the cold reservoir. Thus, if continuous heating and cooling occur, the net work $pdV = 0$. This condition is achieved via the use of channels that are larger than the thermal penetration depth of the gas. Thermal penetration depth, δ_k , is defined as the distance that heat can travel through a gas at a certain frequency, as illustrated in Equation 1.1, where k is the thermal conductivity, ρ is the density, c_p is the coefficient of heat capacity, and ω is the angular frequency of the sound wave. The thermal penetration depth is typically compared to the hydraulic diameter, r_h , of the channels used in the stack, calculated using Equation 1.2, where A is the area, and Π is the perimeter of the channel [13].

$$\delta_k = \sqrt{\frac{2k}{\rho c_p \omega}} \quad (1.1)$$

$$r_h = \frac{A}{\Pi} \quad (1.2)$$

Standing wave engines, while simple, suffer a drawback in efficiency due to the irreversibility of the heat transfer process. The non-isothermal heating and cooling that are isolated by the adiabatic movement impair the efficiency of the standing wave engine to around 20% [14]. Theoretically, due to this irreversibility, standing wave engines also cannot achieve the Carnot efficiency, while, as discussed below, traveling wave engines can.

1.2.2 Traveling Wave Engines

Traveling wave engines are, in general, slightly more complicated in design. Several designs have been proposed and tested, with the more common ones shown in Figure 4. It can be seen that each design employs a looped compliance, proposed and tested by first Ceperley [8], then Backhaus et al. [15] and Ueda et al. [16], or a feedback inertance, first employed by deBlok [17].

As aforementioned, the traveling wave thermodynamic cycle follows the same steps as the Stirling cycle. The cycle begins with gas under high pressure moving toward the hot reservoir, absorbing heat and slightly expanding along the way. Here, the gas absorbs heat

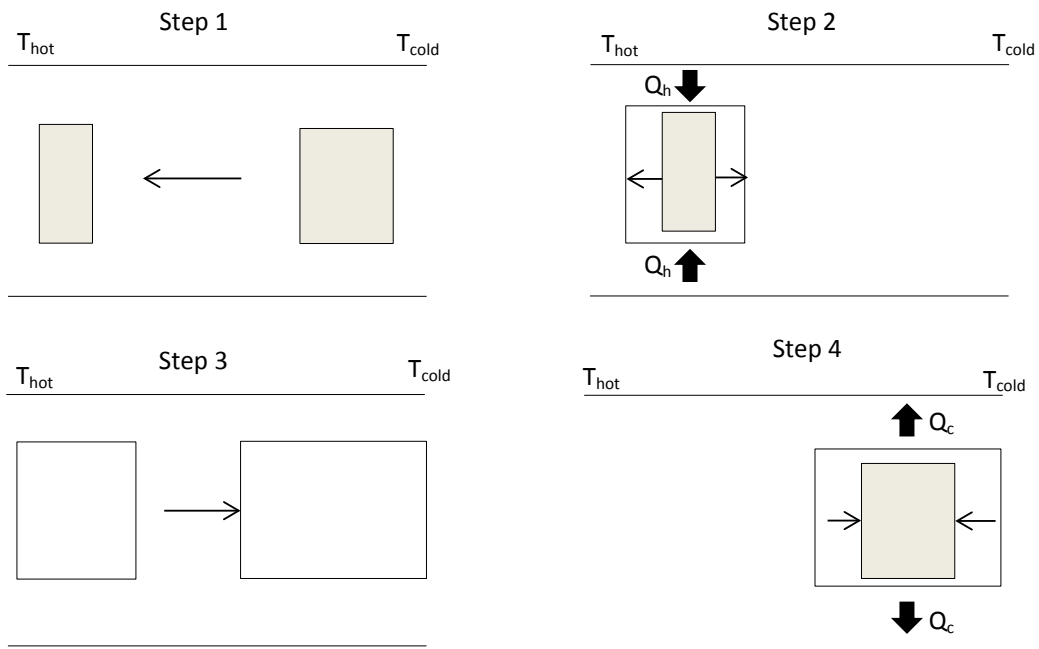


Figure 2: Standing wave TAE cycle

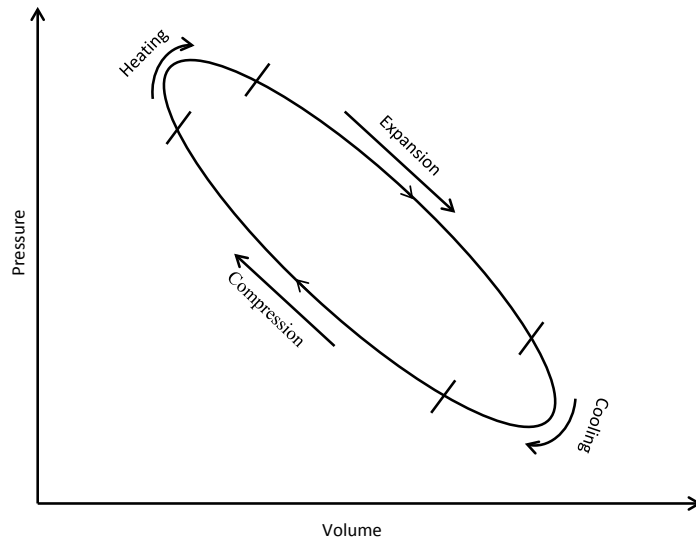


Figure 3: Standing wave TAE P-V diagram corresponding to cycle shown in Figure 2.

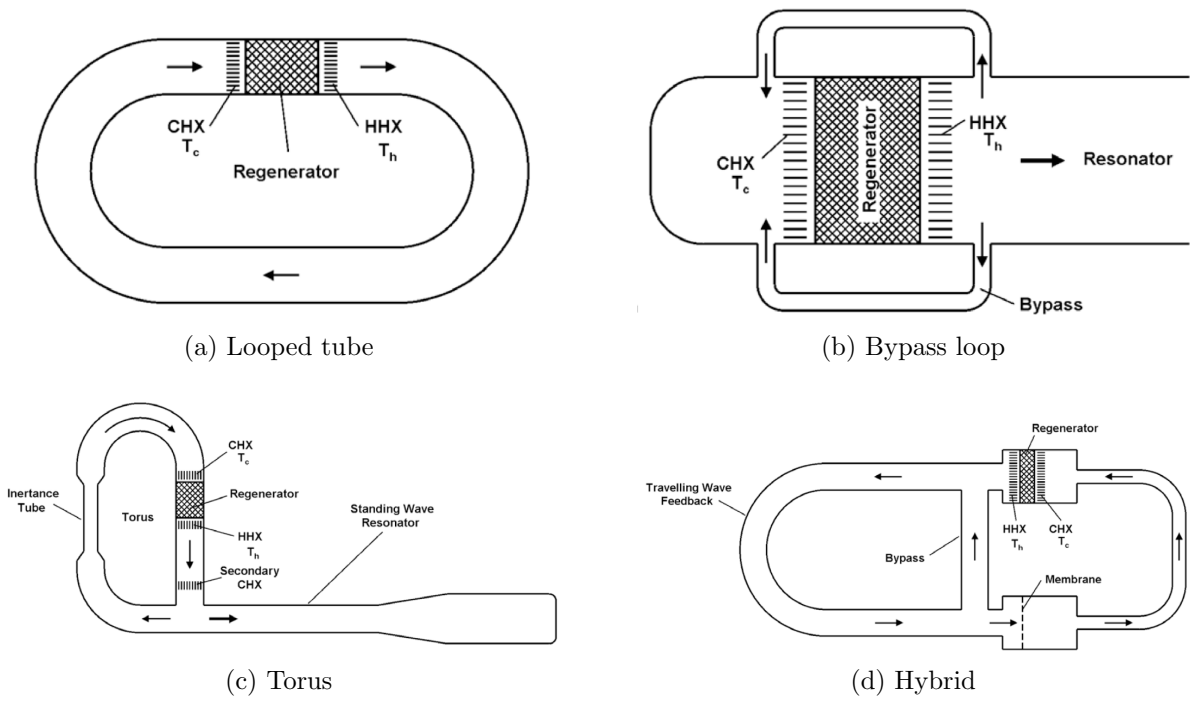


Figure 4: Various traveling wave engine designs [18]

from the regenerator that was stored from the previous cycle. Ideally, this step is assumed to be isochoric. The gas then expands from falling pressure at the hot reservoir, dropping in temperature and absorbing surrounding heat. In the ideal approximation of this step, it would be assumed that the process is isothermal. The gas is then moved toward the cold reservoir, releasing heat to the surroundings and undergoing some thermal contraction. This step again would ideally be isochoric and is the complement to the first step, allowing for latent heat to subsequently be drawn from the regenerator. Finally, the gas is compressed, simultaneously rejecting heat to the cold reservoir. Similar to the second step, it can be assumed for the ideal case that this step is also isothermal. Figures 5 and 6 show the individual steps and the pressure and volume relationship, respectively.

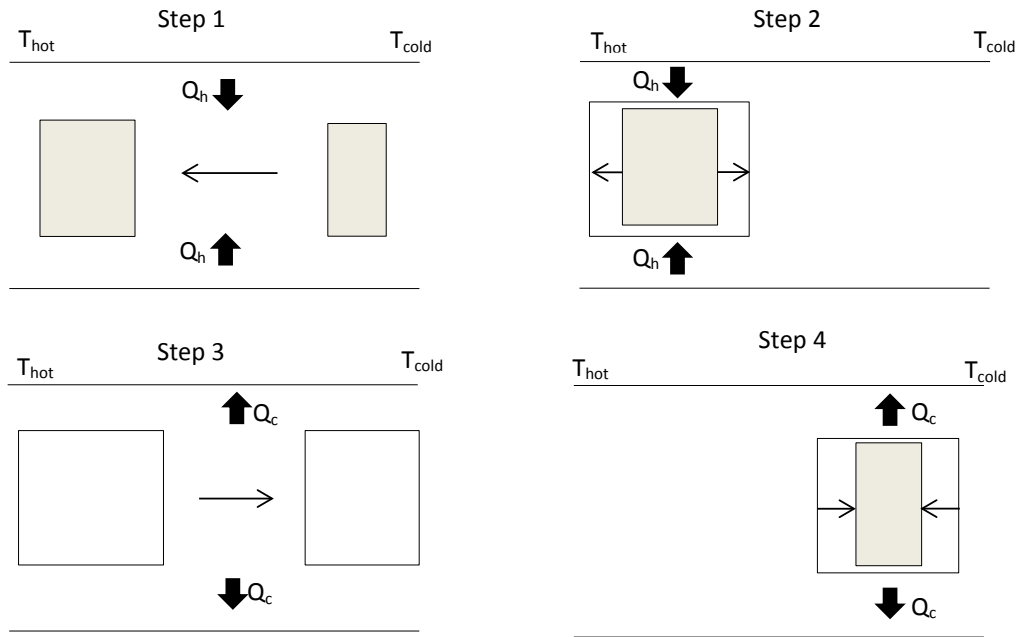


Figure 5: Diagram of a traveling wave cycle

Traveling wave engines are designed to operate with the pressure and velocity oscillations in phase, allowing for the maximum rate of compression or expansion to occur at the peak left- or rightmost displacement. This behavior eliminates the need for adiabatic movement of the gas, changing the function of the stack to that of a regenerator rather than a heat

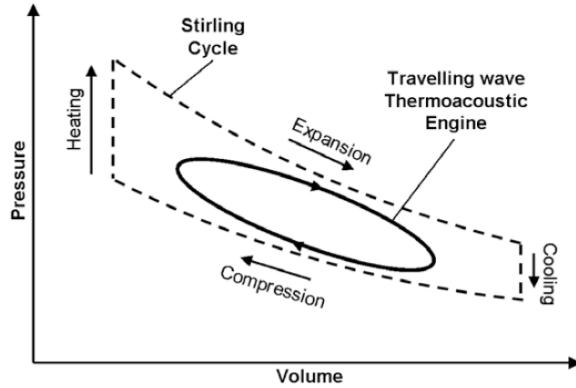


Figure 6: Traveling wave TAE P-V diagram corresponding to cycle in Figure 5 [18].

storage surface. The design of a traveling wave engine then requires for the channels to be significantly smaller than that of a standing wave engine, particularly small enough to where $\delta_k \gg r_h$. This allows for nearly isothermal heat transfer through the cycle, allowing for the traveling wave engine to theoretically be capable of reaching the Carnot efficiency.

1.3 MOTIVATION FOR THERMOACOUSTIC REFRIGERATION

The widest application of thermoacoustics can be seen today in its use in refrigeration and cryogenic cooling. Most cooling demands are currently met via the use of vapor compression and absorption cooling. However, TARs have several advantages over these systems, as discussed below, that can help them increase their share in the market in an environmentally sustainable way.

1.3.1 Absorption Cycles

Absorption cycles employ the use of a chemical solution to drive mixture and separation of typically two compounds, such as water and lithium bromide. The use of two solutions

allows for evaporated water at low pressure to be absorbed into the solution, pressurized using a low amount of energy, and again evaporated, recycling the lithium bromide solution. The highly pressurized water can be again condensed at a higher temperature and after a decrease in pressure, evaporated at a lower temperature to begin the cycle again. Figure 7 shows a simple diagram of an absorption cycle.

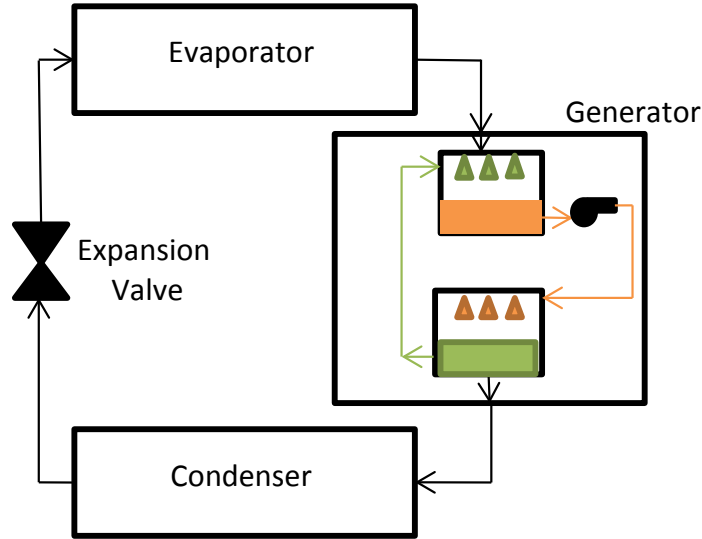


Figure 7: Diagram of a typical absorption cycle

The major inputs of energy for absorption cycles are electric or shaft power into the pump to bring the solution to a high pressure and heat at high pressure to evaporate the liquid. Here, the absorption cycle has an advantage in the use of heat rather than mechanical energy, as compared to the vapor compression cycle discussed below. Thus, a lower exergy source of energy can be used to drive this cycle, such as waste heat from an industrial process, heat given off by a combustion engine, or solar energy. Absorption cycles, however, suffer from several drawbacks. They are much more complex than either vapor compression systems or TARs and have a relatively low COP, typically around 0.68 for partially solar powered cycles [19]. Additionally, when liquids such as ammonia are used in absorption cycles, extra care must be taken if the solution leaks since ammonia is an environmentally dangerous chemical.

1.3.2 Vapor Compression

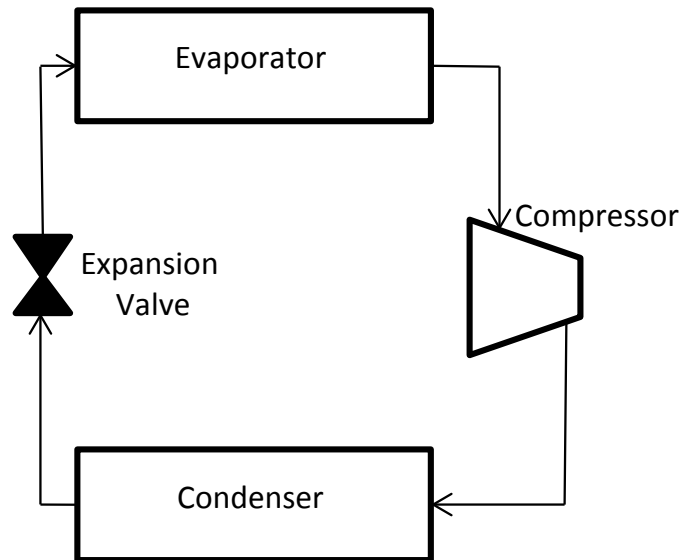


Figure 8: Diagram of a typical VC cycle

Vapor compression (VC) is currently the dominant form of refrigeration, found in a range of applications, from household air conditioners to industrial ice makers and gas liquification. The VC cycle is very simple in its design, employing four basic stages: evaporation, compression, condensation, and expansion, shown in the diagram in Figure 8. Similar to absorption cycles, the evaporation stage is used to achieve cooling and the condenser to release high pressure heat to the ambient air. However, in a VC cycle, the compressor replaces the absorption system, simplifying the process. VC technology, however, has several drawbacks in that it is limited to approximately $230K$ in a single stage and requires high exergy energy (i.e. mechanical or electrical) to operate. This causes a major increase in complexity when temperatures like that of liquid nitrogen and helium are desired. TARs, on the other hand, have been reported to be able to achieve much lower temperatures, with Jin et al. reporting $120K$ [20] and Vanapelli et al. reaching a temperature as low as $50K$ [21].

1.3.3 Thermoacoustic Cooling

Thermoacoustic refrigerators can be assembled in several configurations, using either mechanical, or thermal energy to drive the thermoacoustic effect. TARs have several advantages over the cycles discussed above. Both VC and absorption cycles require the use of potentially dangerous refrigerants and are fairly complex systems, increasing the potential for leaks. TARs benefit from use of inert gases like Helium and Argon, or can even be operated with air, making them simple and safe. They also present a secondary advantage in the use of cryogenic cooling. It is well-known that standard vapor compression refrigerators (VCRs) have a limited lifespan due to the low temperatures the seals experience around the moving parts. TARs bypass this need due to the lack of moving parts in the design. Thus, when space is not limited, such as in cryocooling stations, or on large refrigeration trucks, TARs have the potential to replace the current technology quite readily.

One of the main reasons why TARs have not been implemented on a large scale is based on their inherently low coefficient of performance (COP), which is the ratio of cooling capacity to input energy. Note that the COP is not an efficiency in the classical sense, and is thus not bounded by 1. A benchmark of current cooling technology illustrates a spread of COPs of traditional refrigeration between 2 and 6, varying with different working fluids, compressor efficiencies, and operating temperatures [22]. On the other hand, TARs are still operating at COPs of 1 to 1.2 [23, 24]. Limitations for the COP in TARs come from streaming, acoustic, viscous, and thermal losses [23], which are discussed further in Ch. 2.

Fortunately, though, recent work has found that TARs and thermoacoustic engines (TAEs) can be powered by waste heat, at input temperature levels that are not suitable for powering VCRs [25]. This means that the practical level of the input energy is greatly reduced, thus making waste heat-driven TARs/TAEs competitive with VCRs, since VCRs require mechanical energy (often produced from electrical energy) to power the compressor. However, beyond this COP comparison, another limiting factor for wide spread implementation of thermoacoustics is the physical size of TARs. If the resonator could be coiled as opposed to being designed as a straight tube, the footprint of TAEs and TARs could be reduced, and thus be advanced towards broader implementation. While theoretical models

for curvature behavior in relation to the thermoacoustic effect have previously been proposed [26], there is currently a lack of computational models that accurately predict the phenomenon.

1.4 GOALS OF THIS WORK

In this work, two thermoacoustic devices are designed and evaluated for their performance in relation to pressure and temperature. A standing wave thermoacoustic device is designed to establish temperature behavior patterns for the hot and ambient sides and compare the temperature difference across the stack to the magnitude of pressure oscillations in the engine. A traveling wave engine is then designed and evaluated for temperature behavior through the regenerator to establish the intensity of the thermoacoustic effect via the temperature difference.

2.0 THERMOACOUSTIC THEORY

2.1 LINEAR ACOUSTIC THEORY

First developed by Nikolaus Rott [27], linear acoustic theory is the first complete theory that fairly accurately predicts behavior of thermoacoustic engines and refrigerators. While Kramers [6] developed his theory before Rott, his derivation was based on the assumptions of linearization of all equations and the boundary layer approximation. These were not able to provide accurate predictions, leading Rott to further specify the problem by defining the following assumptions:

- (1) The gradient of the acoustic pressure in the radial direction is assumed to be zero,
- (2) The average temperature and viscosity in the radial direction are negligible, and
- (3) Axial heat conduction in the medium is negligible in comparison to the thermoacoustic effect, and friction in the axial direction is neglected.

These assumptions are implied from the overall general assumption that the tube radius is significantly smaller than the tube length, a crucial assumption that allowed for Rott to achieve much more accurate predictions for the behavior of thermoacoustic devices. Beginning with the continuity, momentum, and energy equations and assuming that u and v undergo time variation given by the factor $exp(i\omega t)$, the equations become, respectively:

$$\omega\rho + \rho_m \frac{\partial u}{\partial x} + u \frac{d\rho_m}{dx} + \rho_m \frac{\partial(r^j v)}{r^j \partial r} = 0 \quad (2.1)$$

$$i\omega u + \frac{1}{\rho_m} \frac{dp}{dx} = \nu \frac{1}{r^j} \frac{\partial}{\partial r} \left(r^j \frac{\partial u}{\partial r} \right) \quad (2.2)$$

$$\rho_m c_p \left(i\omega T + u \frac{dT_m}{dx} \right) - i\omega p = \frac{\mu c_p}{\sigma} \frac{1}{r^j} \frac{\partial}{\partial r} \left(r^j \frac{\partial T}{\partial r} \right) \quad (2.3)$$

where ν is the kinematic viscosity, σ is the Prandtl number, and j can be either 0 or 1, depending on if the solution is for the plane or axisymmetric case, respectively. By combining the above three equations, applying the boundary conditions, and redefining some of the variables, the equation for pressure is achieved:

$$[1 + (\gamma - 1)f_j^*]p + \frac{d}{dx} \left[\frac{a^2}{\omega^2} (1 - f_j) \frac{dp}{dx} \right] - \frac{a^2}{\omega^2} \frac{f_j^* - f_j}{1 - \sigma} \theta \frac{dp}{dx} = 0 \quad (2.4)$$

where θ describes the gradient of the mean temperature, f_j and f_j^* correspond to the wall gradients, and $a^2 = \gamma RT_m$.

Arnott et al. developed on these forms to create relations for the heat and work flow [28]. He began with the average energy flow over time:

$$\bar{H}_2(z) = \bar{Q}_2(z) + \bar{W}_2(z) - \bar{Q}_{loss}(z) \quad (2.5)$$

where the heat flow due to the hydrodynamic contribution is:

$$\bar{Q}_2(z) = \frac{\Omega A_{res}}{2} Re \frac{1}{A} \int_A [\rho_0 c_p v_z(x, y, z) T_1^*(x, y, z) - \beta T_0 v_z(x, y, z); P_1^*(z)] dx dy \quad (2.6)$$

The heat flow due to conduction is defined as:

$$\bar{Q}_{loss}(z) = \Omega A_{res} k_{gas} T_{0z} + (1 - \Omega) A_{res} k_{stack} T_{0z}; \quad (2.7)$$

and the averaged work flow over time (i.e. power) is:

$$\bar{W}_2(z) = \frac{\Omega A_{res}}{2} Re \frac{1}{A} \int_A v_z(x, y, z) P_1^*(z) dx dy. \quad (2.8)$$

A_{res} is defined as the cross-sectional area of the tube at a point z , A is the area of a single pore, Ω is the porosity of the stack, k_{gas} and k_{stack} are the thermal conductivity values for the the gas and stack, respectively, $*$ defines complex conjugation on the variable in question, and Re indicates that the real part of the expression is being evaluated.

To develop the above relations to a functional form, the velocity in the z direction was defined as:

$$v_z(x, y, z) = \frac{F(x, y; \lambda)}{i\omega\rho_0} \frac{dP_1(z)}{dz} \quad (2.9)$$

where $\lambda = 2^{1/2}R/\delta_v$ and $F(x, y, ; \lambda)$ is a function that equals zero at the wall. The heat and work flow then took the following form:

$$\bar{Q}_2(z) = \frac{\Omega A_{res}}{2} \beta T_0 \left[Im \left(\frac{P_{1z}(z) P_1^*(z)}{\rho_0 \omega} \frac{F^*(\lambda_T) - F(\lambda)}{1 + N_{pr}} \right) - \frac{T_{0z}}{\beta T_0} \frac{c_p}{\rho_0 \omega^3} |P_{1z}(z)|^2 \frac{Im[F^*(\lambda_T) + N_{pr} F(\lambda)]}{1 - N_{pr}^2} \right] \quad (2.10)$$

$$\bar{W}_2(z) = \frac{\Omega A_{res}}{2} Im \left(\frac{P_{1z}(z) P_1^*(z)}{\rho_0 \omega} F(\lambda) \right) \quad (2.11)$$

Tijani et al. continued the development of the theory to provide heat and work flow equations that are based on dimensionless parameters describing thermoacoustic devices [29]:

$$Q_{cn} = -\frac{\delta_{kn} D^2 \sin 2x_n}{8\gamma(1+\sigma)\Lambda} \left(\frac{\Delta T_{mn} \tan(x_n)}{(\gamma-1)BL_{sn}} \frac{1+\sqrt{\sigma}+\sigma}{1+\sqrt{\sigma}} - (1+\sqrt{\sigma}-\sqrt{\sigma}\delta_{kn}) \right) \quad (2.12)$$

$$W_n = \frac{\delta_{kn} L_{sn} D^2}{4\gamma} \left[(\gamma-1)B \cos^2 x_n \left(\frac{\Delta T_{mn} \tan(x_n)}{BL_{sn}(\gamma-1)(1+\sqrt{\sigma})\Lambda} - 1 \right) - \frac{\sqrt{\sigma} \sin^2(x_n)}{B\Lambda} \right] \quad (2.13)$$

In the above equations, x_n is the center position of the stack, L_{sn} is the length of the stack, A is the cross-sectional area, σ is the Prandtl number, $\delta_{kn} = \delta_k/y_0$ is the normalized thermal penetration depth, D is the drive ratio, γ is the ratio of isobaric to isochoric specific heats, and B is the porosity of the stack. Additionally, $\Lambda = 1 - \sqrt{\sigma}\delta_{kn} + \frac{1}{2}\sigma\delta_{kn}^2$. Tijani et al. used these equations to provide a framework for designing thermoacoustic refrigerators with optimized parameters for the highest COP, acoustic power, or cooling rate [30].

While the general theory of thermoacoustics is well understood, there is still much research being conducted in the study of the losses that occur in TAEs and TARs. Application of Tijani's derivations presents possible COP values as high 1.8 for optimized design specifications. However, due to various losses, these values are, in fact, much lower than is theoretically predicted. Acoustic, streaming, and viscous losses have been extensively researched in the past and have been shown to be major contributors to the energetic losses in thermoacoustic devices. These losses will be explained as part of the influencing factors in the behavior of the standing wave device examined in this work. Thermal losses are less understood, as it is harder to quantify their effects due to the parallel nature of their behavior with the thermoacoustic effect. Zink et al. [31, 32] proposed methods for quantifying these losses, showing significant effects due to convection and radiation.

2.2 STREAMING LOSSES

Streaming losses can be identified as the energy losses that are caused by the movement of the gas in the thermoacoustic device. While gas displacement in the stack or regenerator of the thermoacoustic device is crucial to that device's performance, other gas movements have been identified and observed in various devices that are detrimental to the performance. Gedeon and Rayleigh streaming mechanisms have been found to contribute significantly to the overall losses found in thermoacoustic engines and refrigerators, and have been noted to have the largest effect on refrigerators and traveling wave engines.

2.2.1 Gedeon Streaming

Gedeon streaming is defined as the acoustic streaming around a torus. This streaming occurs in traveling wave looped tube engines and pulse tube design refrigerators. The mechanism of this streaming occurs as gas particles travel in the regenerator through a complete cycle. While it would be expected for each particle to assume the original position at the end of each cycle, it is found that the distance that a particle covers from the hot to the cold side

is not the same as in the opposite direction. Thus, a net mass flow, as shown in Figure 9, is experienced and is exacerbated by the fact that there is no hindering mechanism in a torus or pulse tube design to prevent circulation of the particles. This results in a heat transport mechanism that is parallel to the thermoacoustic mechanism, causing a heat load on the cold side and thus decreasing efficiency.

Gedeon streaming has been evaluated by several groups, both experimentally and analytically. Olson et al. [33] have shown the effect of this mechanism in pulse tube refrigerators, demonstrating that its suppression can increase performance. They established that the oscillations approximately a penetration depth away from the pulse tube wall cause a drift, establishing a parabolic mass flux profile, as shown in Figure 10, and causing convection of heat. Using linear acoustic theory, presented above, they were able to establish an expression for the streaming mass flux,

$$\dot{m}_{2,w} = \frac{|p_1||u_1|}{a^2} \left[\left(\frac{3}{4} + \frac{(\gamma - 1)(1 - b\sigma^2)}{2\sigma(1 + \sigma)} \right) \cos\theta + \left(\frac{3}{4} + \frac{(\gamma - 1)(1 - b)\sqrt{\sigma}}{2(1 + \sigma)} \right) \sin\theta \right] + \frac{\rho_m|u_1|^2}{\omega} \left[\frac{3}{4} \frac{dA/dx}{A} + \frac{(1 - b)(1 - \sqrt{\sigma})}{4(1 + \sigma)(1 + \sqrt{\sigma})} \frac{dT_m/dx}{T_m} \right] \quad (2.14)$$

An analytical approach was conducted by Gusev et al. [34], using the measure of enthalpy flux to demonstrate that the mechanism has a significant impact. Other groups, such as Penelet et al. [35] have shown that streaming has a positive effect on thermoacoustic performance, providing amplification of the thermoacoustic effect. Overall, however, there have been numerous efforts to suppress Gedeon streaming.

One method that has been shown to increase performance in engines was proposed by Swift et al. [36]. Their group demonstrated an increase in performance through the use of a flexible membrane inside the torus. This membrane, of course, introduces an acoustic impedance, causing an increase in acoustic losses in the engine. Olson et al. [33] proposed a different method for suppressing streaming using a tapered pulse tube, producing significant results.

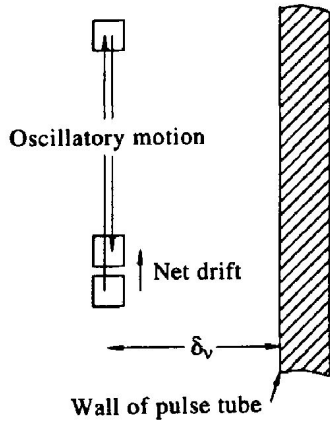


Figure 9: Illustration of net mass flow occurrence in pulse tube [33].

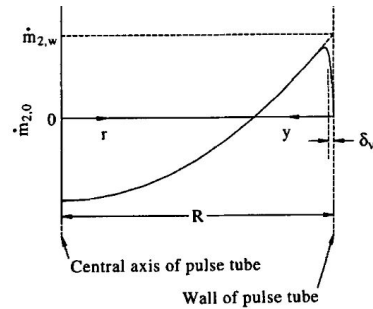


Figure 10: Mass flux profile in pulse tubes from central axis to wall [33].

2.2.2 Rayleigh Streaming

While Gedeon streaming is specific to traveling wave designs, Rayleigh streaming is an occurrence that can be found in both standing and traveling wave engines, and has been shown to be equally significant in refrigerators. This method of streaming stems from the interaction of the oscillating flow and the the various surfaces inside the engine or refrigerator. First proposed by Rayleigh in 1896, this method was investigated by several groups, and was experimentally proven by Gaitan et al. [37]. Yazaki et al. [38] investigated this streaming mechanism further using Doppler velocimetry to examine thermoacoustic work flow. They were able to obtain results that agreed with theory and images, such as Figure 11, to show that the streaming is, in fact, significant.

Thompson et al. [39] used Laser Doppler Anemometry (LDA) and burst spectrum analysis (BSA) to obtain velocity field measurements, such as the one in Figure 12, showing streaming inside a standing wave device. Using these measurements, they were able to show the relationship between the axial acoustic velocity and the axial streaming velocity shown in Figure 13.

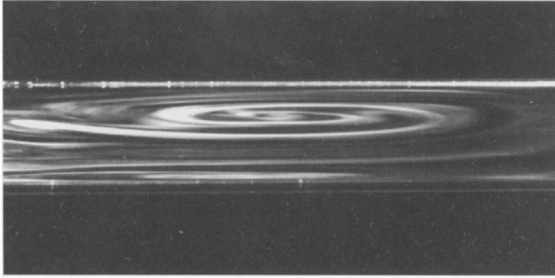


Figure 11: Image of streaming taken using Doppler velocimetry [38].

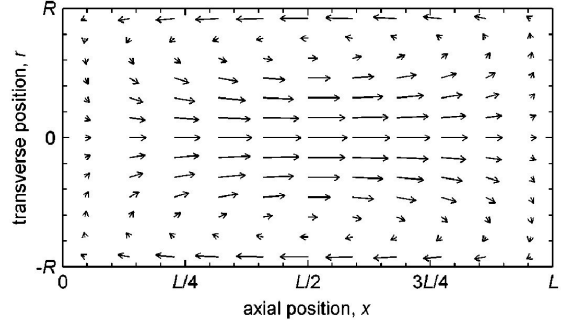


Figure 12: Velocity field observed using LDA and BSA [39].

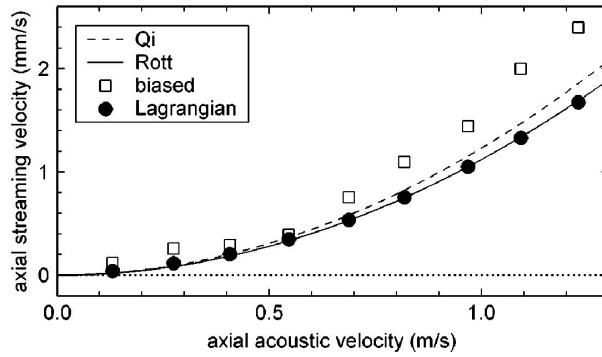


Figure 13: Relation between axial acoustic and axial streaming velocities [39].

2.3 ACOUSTIC LOSSES

There are several mechanisms of acoustic losses that take place in thermoacoustic devices. Resonator shape, uneven joints, and open end conditions can have a significant impact on acoustic wave propagation. A significant amount of research has been conducted on improving the acoustic efficiency of engines. Several groups have identified the use of tapered resonator tubes to help increase performance.

As discussed above, there are several loss mechanisms that cause a decrease in performance, and solutions to decrease the effects of some losses will cause other losses to increase. This is particularly true in refrigeration, where it is beneficial to separate driving and refrigeration stacks to decrease/eliminate convective losses. In both traveling and standing wave refrigerators, this increases the complexity of the design and can create a large increase in impedance caused by the resonance body.

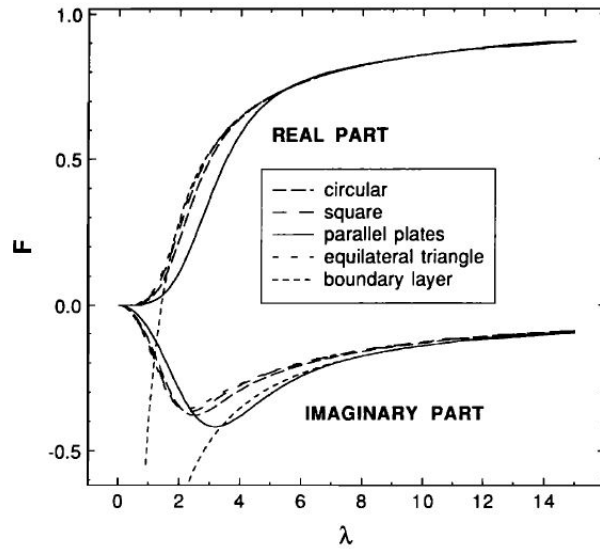


Figure 14: Real and imaginary parts of $F(\lambda)$ for various pore geometries [28].

Stack design has also been examined. Arnott et al. [28] analytically examined work and heat flows for various pore geometries using equations 2.10 and 2.11. They determined that the primary influence on the work and heat flow is the function $F(\lambda)$. Thus, they evaluated

this function for both its real and imaginary parts for various values of λ . As shown in Figure 14, parallel plate stacks have the largest imaginary part at a value $\lambda_c \approx 3.2$, demonstrating that they will produce the strongest thermoacoustic effect.

2.4 VISCOUS LOSSES

It is well-known that movement of a fluid will experience viscous energy dissipation and, in some cases, a significant amount of viscous heating. This form of energy dissipation is clearly present in stacks/regenerators, as the large surface area to volume ratio causes the presence of significant dissipation through both methods. Atchley et al. [40–42] have shown that these two forms of energy dissipation are, in fact, the dominant mechanisms in thermoacoustic devices. They presented the following form for calculating the losses in the heat exchangers

$$d\dot{W}_{hx} = \frac{1}{2} S_{hx} Re \left\{ \frac{P_A^2 \omega}{\rho_m a^2} i \left[\left(1 + \frac{(\gamma - 1)}{1 + \epsilon_s} \bar{f}_k \right) \cos^2 \phi(x) - \frac{(1 + l/y_0)^2}{1 - f_v} \sin^2 \phi(x) \right] \right\} dx \quad (2.15)$$

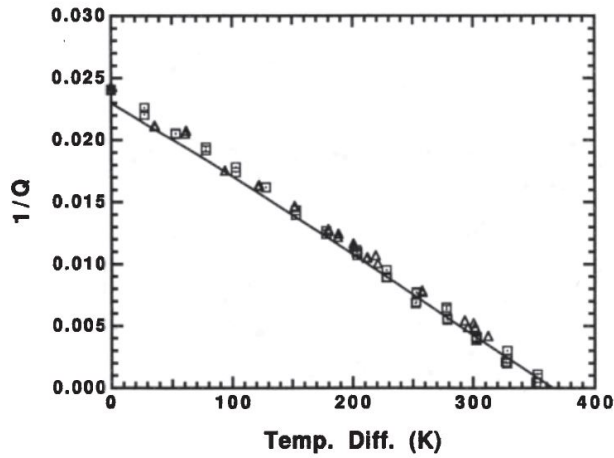


Figure 15: Experimental results compared to analytical forms for heat compared to the temperature difference [40].

where S_{hx} is the cross-sectional area of the heat exchanger, P_A is the peak pressure amplitude, a is the speed of sound, f_k and f_v are function of the thermal and viscous penetration depths, and y_0 is the plate half-spacing. The analytical forms were examined against experimental results for a thermoacoustic prime mover below onset of self-oscillation, shown in Figure 15, providing close agreement between the data and the predictions. In the next section, thermal losses are examined more closely and compared to the viscous losses that were discussed here.

2.5 THERMAL LOSSES

Thermal losses in thermoacoustic devices are less understood than the other mechanisms discussed above. Since, as discussed, thermoacoustic devices operate on the basis of temperature gradients, there will be nontrivial losses due to conduction through the stack as well as convection to the medium. Due to the parallel nature and interaction behavior of the mechanisms, however, it is more difficult to quantify the impact of these losses experimentally.

Losses via conduction have been mentioned in several studies. Organ et al. [43] referred to these losses in their evaluation of mechanical Stirling engines. Referred to as “thermal shorting,” their group discussed how heat flow paths are created in regenerators built from stacked wire meshes. Chen et al. [44] investigated the COP of a thermoacoustic refrigerator with regard to the temperature difference applied across the stack, arriving at a conclusion that the thermal conductivity of the stack noticeably influences the performance. Holmberg et al. [45] used software to determine the significance of several viscous and thermal losses in stacks and on a system level. Their group evaluated a thermally driven thermoacoustic refrigerator consisting of two stacks and three heat exchangers, assembled in a series configuration to achieve cooling at the surface facing the open end of the resonator, as shown in Figure 16. A system level analysis, seen in Figure 17, shows that the cooling work is only a small portion of the overall thermal input. Due to the design used in the analysis, the largest portion was found to be in the viscous losses of the high temperature heat exchanger with the viscous thermoacoustic losses becoming a close second at high heat input. An analysis of the heat exchanger control volume, shown in Figure 18, showed a significant amount of

thermal loss due to the conduction in the stack, indicated as $Q_{cond,1avg}$, despite the stack being designed using ceramic material.

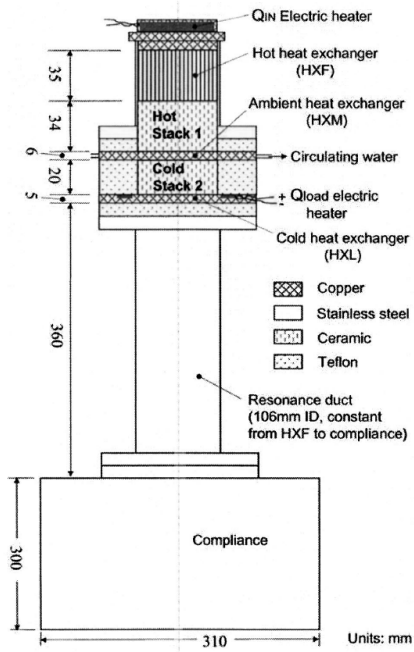


Figure 16: TAR design [45]

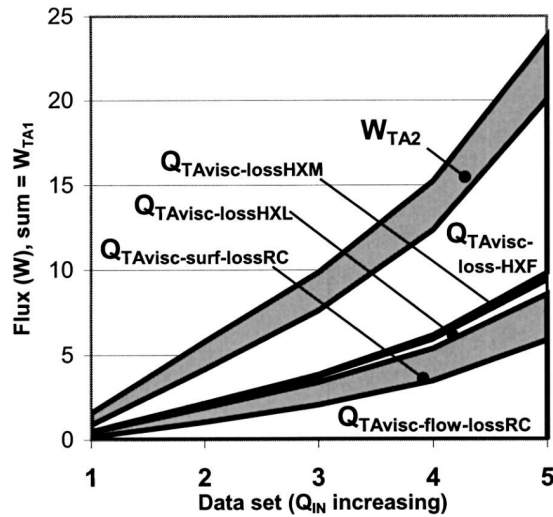


Figure 17: Thermoacoustic refrigerator thermal and viscous losses [45].

Holmberg's group presented an estimate for the magnitude of losses in the thermoacoustic refrigerator, including conduction loss through the ceramic stack. A thorough investigation in how this loss varies with stack materials was presented by Zink [32, 46] in his investigation of conductive, convective, and radiative losses for aluminum, stainless steel, copper, ceramic, and brass stacks. Using a quarter-wavelength thermoacoustic engine, he evaluated the acoustic performance with respect to input power, as seen in Figure 19. Ceramic stacks were found to perform significantly better than other materials. However, an evaluation of convective and radiative losses, seen in Figures 20 and 21, presented a drawback of the lower conduction material in the increase of the temperature at the hot side and increase in both convection and radiation.

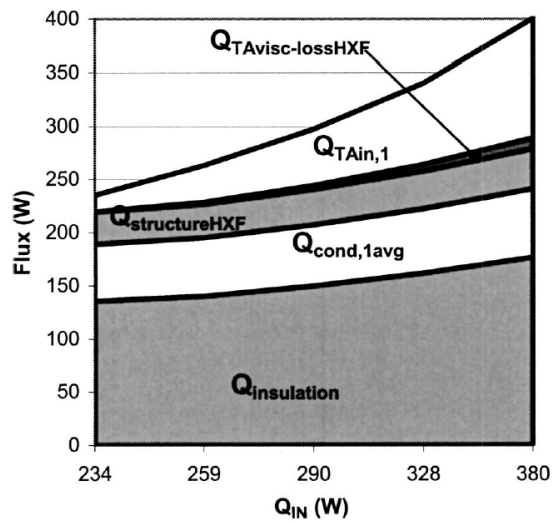


Figure 18: TAR hot side exchanger thermal and viscous losses [45].

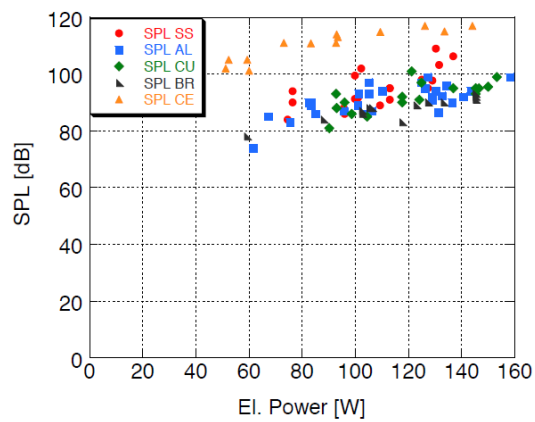


Figure 19: TAR hot side exchanger thermal and viscous losses [32].

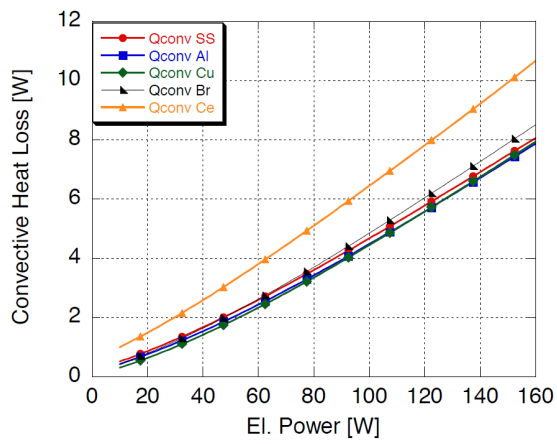


Figure 20: Convective losses [32]

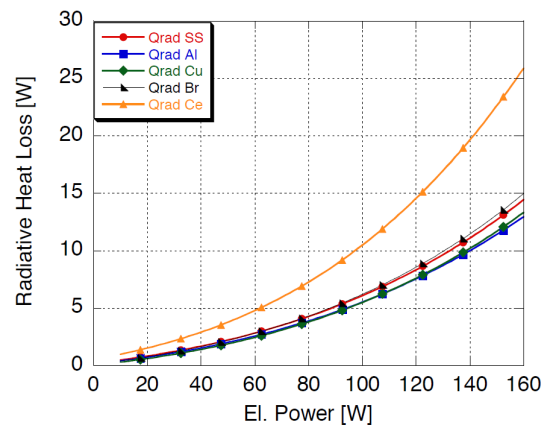


Figure 21: Radiation losses [32]

3.0 STANDING WAVE INVESTIGATION

As discussed in the previous chapter, although recent research has increasingly focused on thermal behavior of thermoacoustic devices, much more work needs to be done. Additionally, as mentioned in Chapter 1, for thermoacoustic devices to be competitive in the marketplace, their efficiency must be improved while increasing the flexibility of their operating footprint. To that end, the goal of this work is to perform experimental investigations to determine:

- (a) how curvature affects the total temperatures on the hot and cold side, and
- (b) how curvature affects the oscillation behavior (i.e. does sound pressure level decrease as curvature increases).

3.1 DESIGN AND CONSTRUCTION

3.1.1 Stack Length and Position

As mentioned above, the quarter-wavelength resonator design operates with a pressure node at the open end of the resonator and an antinode at closed end. Simultaneously, the velocity operates 90° out of phase with the pressure, resulting in a node at the closed end of the resonator. As discussed above, both pressure and velocity oscillations are required for the standing wave cycle to operate. Thus, stack positioning at either end of the resonator does not facilitate effective acoustic generation. Studies on thermoacoustic refrigeration optimization [25, 30] show that it is most efficient for the stack position to be close to the pressure antinode. Tijani et al. [30] have also shown that as stack size increases, the optimal center position of the stack moves further from the pressure antinode. Their group

has also shown that the COP increases and the acoustic power decreases as stack length decreases. Both groups derived optimization methods, Tijani's group's method based on cooling and acoustic power and Babei and Siddiqui's method [25] on cooling power and cold side temperature. Babei and Siddiqui's group has also shown that many similarities can be drawn between TARs and TAEs, allowing for the above mentioned relationships to be applied for TAEs.

These guidelines were implemented in the design of the stack and positioning, for creation of a standing wave device for experimental testing. Due to the brittle nature of the ceramic, a stack length of 2 inches was chosen, corresponding to a normalized length of 0.05. Due to the thermal sensitivity of the microphone, the center positioning of the stack was chosen to be approximately 5 inches, corresponding to a normalized distance of 0.125. For the goal of this study, an optimal stack length and position were not identified, as the curvature of the resonator would affect these parameters in ways not well understood.

3.1.2 Pore Geometry and Size

The stack was chosen from a readily available ceramic monolith with square channels. Several sizes were available, and thus it was important to choose a stack that would meet the requirements of a standing wave engine. To achieve the adiabatic requirement, there must be poor thermal contact between the stack and the working fluid. Using air as the working fluid, and the nominal frequency of $80Hz$, it was determined that the thermal penetration depth was $0.332mm$. A stack with square channels of $1.45mm$ was chosen as an initial size. The ratio of the hydraulic radius to the thermal penetration depth was found to be 1.09, which agreed with the requirement for the operation of standing wave engines, allowing the use of the stack in the engine design.

3.1.3 Resonator

The resonator was chosen for the engine to operate as a quarter-wavelength engine. For a $80Hz$ wavelength, this corresponded to a length of the $1000mm$. The assembly was constructed using a stainless steel stack housing and flexible PVC tubing of $3.9mm$ thickness

(the inner diameter of both was 52.5 mm). The two components were joined by a flange with the stainless steel portion closed at the end and the flexible tubing left open. The flexible PVC tubing was used to acquire the proper curvatures (0° , 15° , 30° , and 45°), precalculated using simple geometry and mounted horizontally. To prevent deformation of the flexible tubing while bending, the maximum curvature was limited to 45° . The assembly was mounted such that the open end would face an unimpeded volume of air at atmospheric conditions of at least 1 meter in radius from the open end. The curved section was constructed to be approximately 500 mm in length, following the model shown in Figure 22.

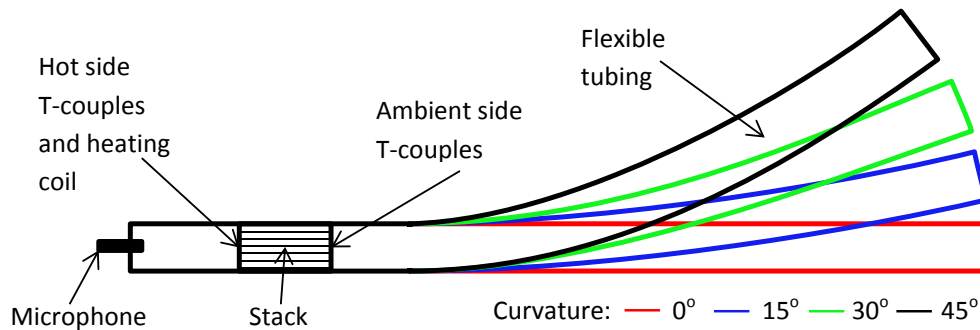


Figure 22: Diagram of standing wave device used in testing

3.1.4 Data Acquisition

The stack was heated with 22-WG nickel-chrome wire and an DC power source. It was mounted in the pattern of a heating coil, shown in Figure 23. Its resistance was $R_H = 2.25\Omega$ (measured at room temperature). During testing a constant voltage input of 15 V was passed through the wire. To record temperatures, four K-type thermocouples were inserted and cemented into each end of the stack. Hot side thermocouples were mounted equidistant from the sides of the coil and approximately 1.5 mm into the stack. Figure 23 shows the position for the hot side thermocouple mounting. The ambient side thermocouples were mounted in a pattern similar to the hot side. Sound output was recorded with a PCB 130D20 array microphone that was mounted in the center of the closed end of the tube. The data acquisition was performed in LabView. The sound pressure level was recorded

simultaneously with the temperature to observe any correlation that they would show. The output of each curvature was recorded in three separate 300 second (5 minute) spans with a sample rate of 0.1 seconds. Each curvature was tested three times to increase the confidence in the temperature and sound pressure level readings. Each test was executed by starting the engine from ambient conditions, allowing it to approach steady behavior, and running the testing interval. A 5V initial run was examined for the transient response from ambient temperature, shown in Figure 24. An exponential fit was applied to the data and a time constant of $\tau_{5V} = 85.4$ seconds was identified for the transient response. The 5V test showed a temperature increase of $102^{\circ}C$, approximately 1/3 in magnitude of the 15V results, shown in the next section. As the magnitude of temperature increase matched the magnitude of voltage input, similar behavior was assumed, implying a time constant of approximately 3 times greater than the 5V test run time constant. With this information, a startup time of 20 minutes was used for the 15V tests, corresponding to 4.7 time constants ($\tau_{15V} \approx 255$ seconds). It was later observed that slower time constants appeared to additionally affect the engine, causing small transient changes in each run. These are assumed to be due to the heating of the housing.

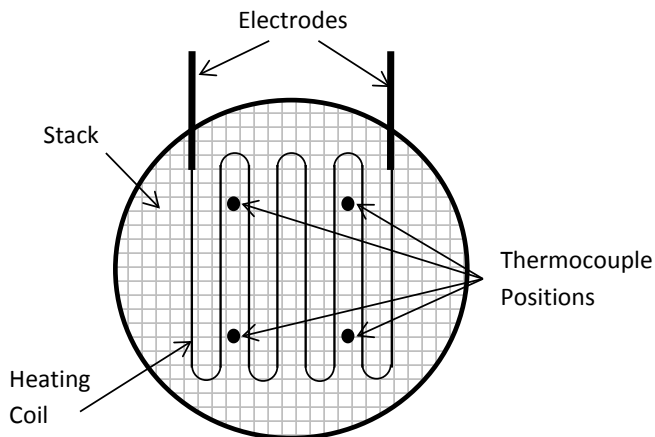


Figure 23: Diagram of hot side of stack assembly

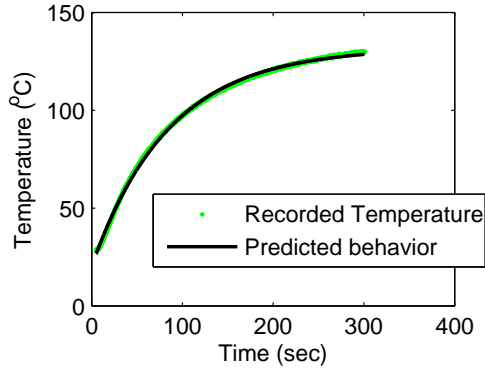


Figure 24: Initial response of SWTAE to 5V input

3.2 RESULTS: TEMPERATURE BEHAVIOR

In order to show the effect of resonator curvature on the thermoacoustic effect, we averaged the recorded readings of the four hot and ambient thermocouples, first for the individual runs, as seen in Figure 25 with the hot side temperature on the top, the ambient side temperature in the middle, and the SPL on the bottom, then the three runs together, displayed in Figures 27 and 29, acquiring an overall average for each curvature. A frequency of occurrence study was conducted for each side, seen in Figures 26 and 28. Finally, a single value average hot and ambient side temperature was calculated at 95% confidence and a regression analysis was performed to quantify a relationship between temperature and curvature, as seen in Figures 30 and 31. The temperature trends seen in these figures are discussed below.

3.2.1 Hot Side Behavior

The range of the individual hot side run averages spans approximately 18°C. The individual runs also show a general trend of increase in temperature with curvature. While this general trend is visible, there is obvious overlap in the averages of the individual runs, particularly between the 0° curvature and 15° curvature. Due to this difficulty, the individual run temperature values were evaluated in a histogram to observe the temperature occurrence

behavior, as seen in Figure 26. The histogram shows that individual runs clearly show peaks in frequency with each curvature, with the 45° and the 15° curvatures showing single peak behavior, and the 0° and 30° curvature showing two peak behavior. To better define the relationship between curvature and hot side temperature, the individual runs were averaged and displayed in Figure 27. The relationship of temperature with time appears relatively horizontal, implying that the hot side achieves steady state. The spacing between the averages stays fairly equal, and thus, a linear relationship can be predicted. The results of a linear regression analysis are discussed below.

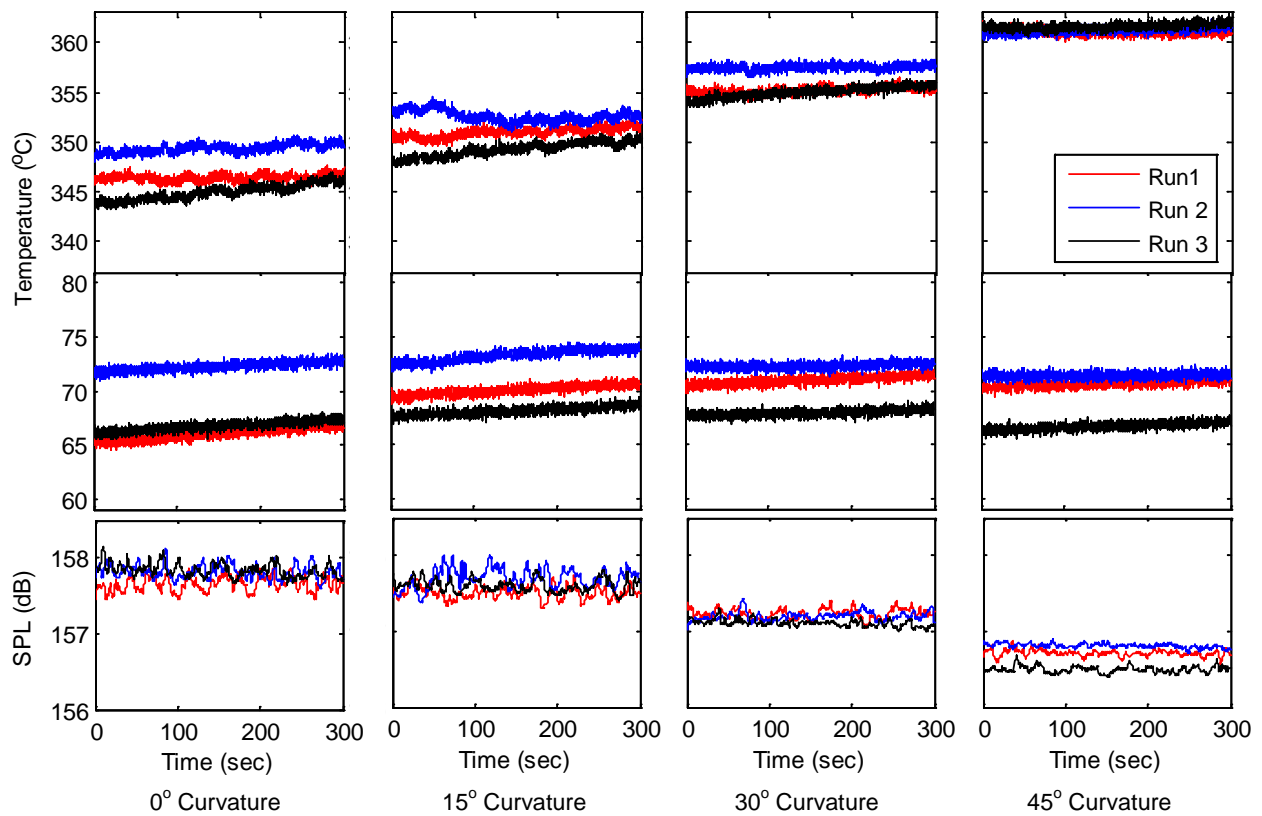


Figure 25: Hot and ambient side temperature and SPL results for each of 3 runs for all curvatures

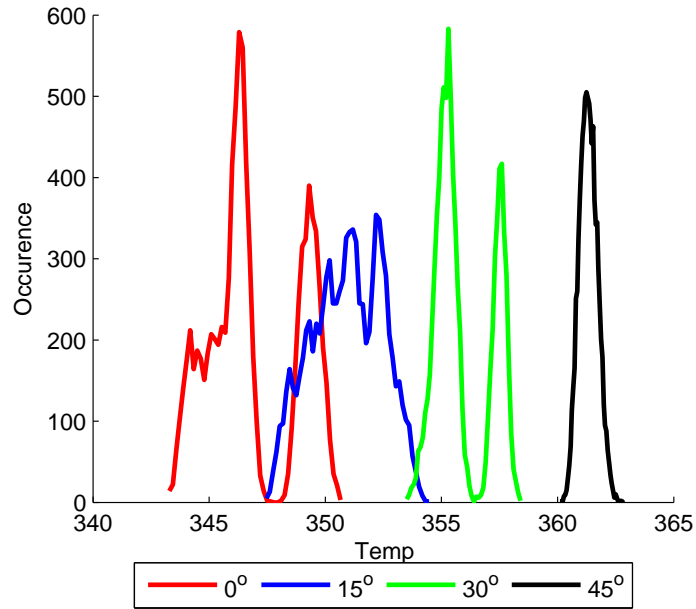


Figure 26: Hot side average histogram for each curvature.

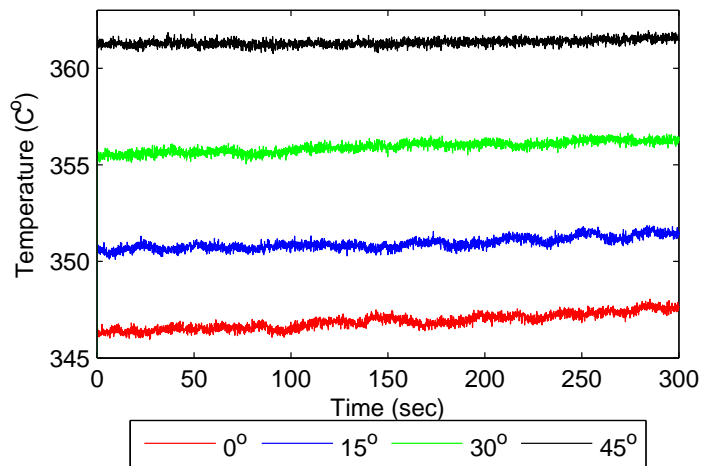


Figure 27: Hot side averages for each curvature

3.2.2 Ambient Side Behavior

The ambient side individual runs fail to show any meaningful pattern, spanning a range of approximately $7^{\circ}C$. A general increase in temperature with time appears for several of the individual runs. A histogram analysis of the temperatures, shown in Figure 28, shows that there is significant overlap and multiple peak behavior for each curvature. An analysis of the average ambient side behavior in Figure 29 shows that the 0° curvature shows the largest increase in temperature with respect to time. The other curvatures also show a pattern of increase with time, but appear to be more horizontal. From this, it can be concluded that the ambient side did not achieve full steady state behavior during the runs as was originally expected. A possible reason for this could be the gradual heating of the stack and the steel housing, due to the leaching of heat from the hot side. A weak trend can be predicted based on the 15° , 30° , and 45° curvatures of decreasing temperature with respect to an increase in curvature. As discussed below, this trend is further evaluated using a regression analysis.

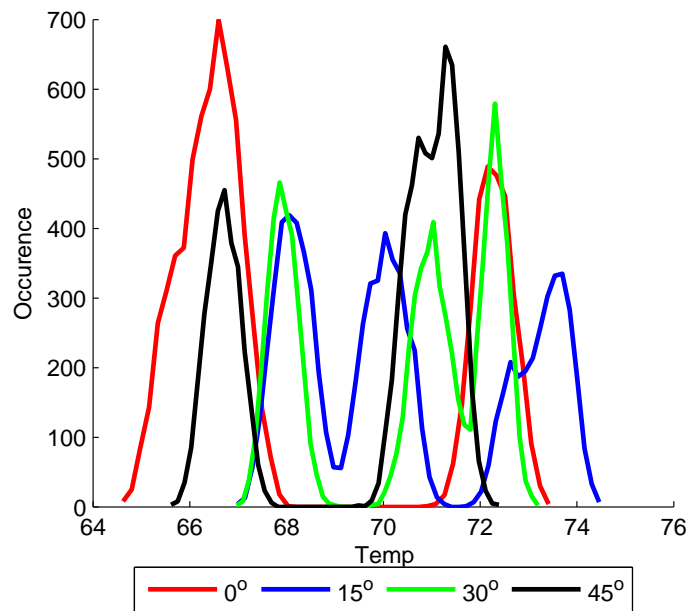


Figure 28: Ambient side average histogram for each curvature.

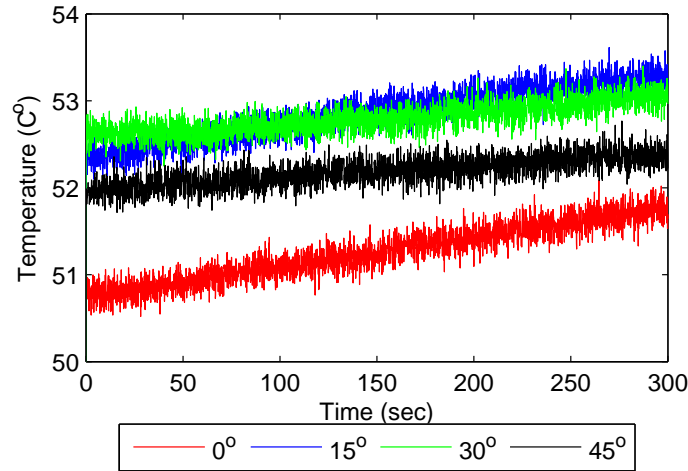


Figure 29: Ambient side averages for each curvature

3.2.3 Trends Between Temperature and Curvature

To better quantify the relationship between average hot side temperature and curvature, an analysis of the total averages for each curvature was performed and displayed with the predicted error of each curvature at 95% confidence, as seen in Figures 30 and 31. The analysis shows a very strong correlation between the curvature and the average hot side temperature with an R-squared value for the relationship of 0.9959. The overall spread of the error in the prediction stays at an acceptable level for each curvature and does not show any major change between curvatures. A similar analysis was performed on the ambient side average temperatures. However, unlike the hot side, the ambient side showed little correlation between curvature and temperature. The average value for the 0° curvature appears to be significantly lower than that of the other curvatures. An analysis of the values for the remaining curvatures produces a relatively strong correlation, with an R-squared value of 0.8129. However, this value does not account for the significantly large spread of error in the values, thus reducing the validity of any relationship present in the ambient data.

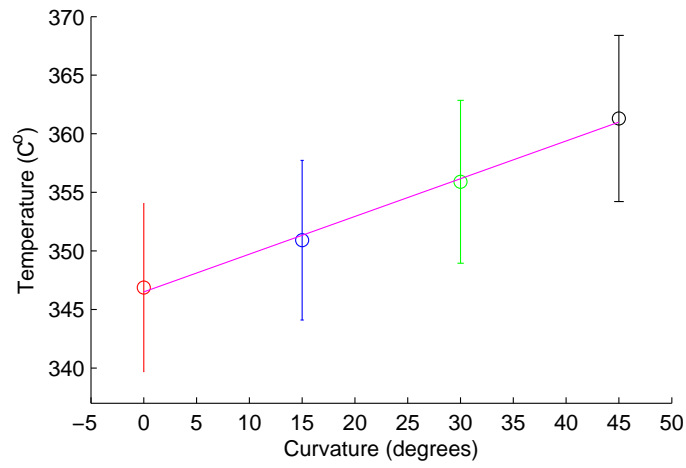


Figure 30: Hot side overall averages with linear regression prediction.

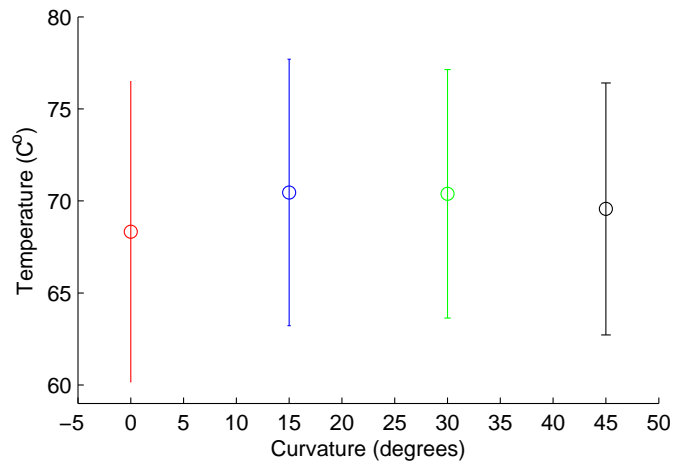


Figure 31: Ambient side overall averages.

3.3 RESULTS: ACOUSTIC BEHAVIOR

Above, we discussed the effect of resonator curvature on the temperature throughout the stack. Next we must discuss the effect of curvature on the pressure behavior of each TAE design as the sound output is the primary metric in the characterization of thermoacoustic devices.

3.3.1 General Oscillation Behavior

As mentioned above, the Sound Pressure Level (SPL) was recorded simultaneously with the temperature behavior. Figure 25 shows the individual recorded levels for each run. While an overall decrease in the pressure level is present, there is significant overlap between the 0° and the 15° curvatures. The overlap between other curvatures is minimal. The SPL data spanned a range of $\approx 2dB$, with a minimum of approximately $156.4dB$, corresponding to pressure amplitudes between 1300 and $1600Pa$. Averaging the runs for each curvature produces a better defined pattern of decreasing SPL with curvature. While the relative spacings between the 15° and 30° curvatures and 30° and 45° curvatures appear approximately equal, the spacing between the 0° and 15° curvatures is significantly smaller. This behavior presents a difficulty in predicting a relationship between SPL and curvature, which is discussed below.

3.3.2 Trends Between SPL and Curvature

The SPL was averaged to a single point for each curvature with error at 95% confidence. No immediate linear relationship was clear, and thus both linear and quadratic predictions were tested. The linear prediction showed a very good correlation of 0.958. However, the quadratic prediction shown in Figure 34, showed a nearly perfect correlation of 0.998, thus implying a quadratic relationship between curvature and SPL, at least for this limited data set. This data has been collected only on a limited span of curvatures and so this relationship cannot be extrapolated to increased curvatures, such as 90° or more. Also, the amount of error present in the data suggests that the relationship, however well defined, may prove unreliable, due to the large amount of overlap of the error.

The sound and hot side temperature behavior both provided the expected relationships. It was thus of importance to evaluate the interaction between temperature and acoustic pressure. The difference in temperature between the hot and ambient sides was evaluated against the acoustic pressure, as shown in Figure 35. A strong relationship can be seen between the temperature difference and the acoustic pressure, showing a linear decrease of acoustic pressure with increase in the temperature difference. This behavior is expected as the temperature difference between the hot and ambient sides of the stack is inversely proportional to the amount of energy transfer that is occurring. A large difference in temperature implies low energy transfer and a lower presence of the thermoacoustic effect. Similarly, a smaller temperature difference implies higher energy transfer. It can be concluded that the relative intensity of the thermoacoustic effect, identified with pressure amplitude (and thus acoustic power), can be measured using a temperature difference across the stack. These findings are utilized in the investigation of the traveling wave engine described below.

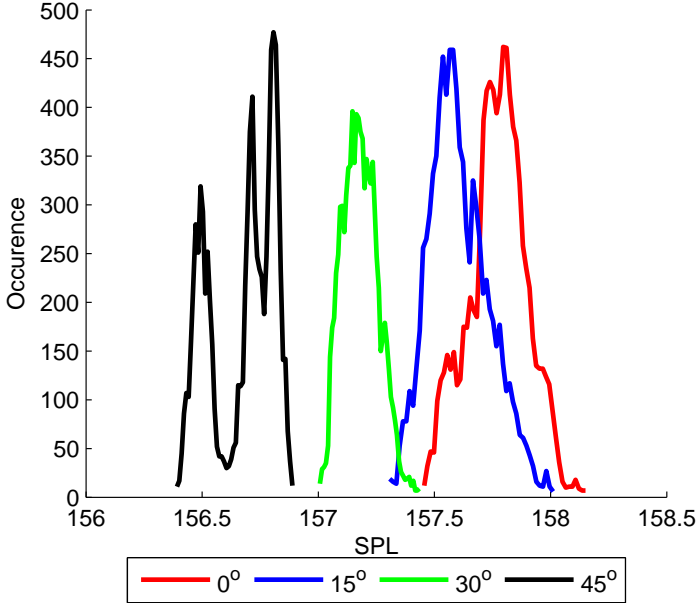


Figure 32: Sound Pressure Histogram

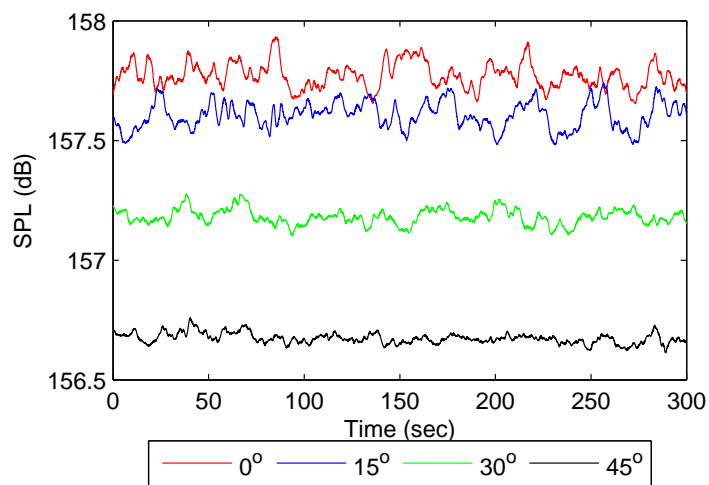


Figure 33: Average SPL for each curvature.

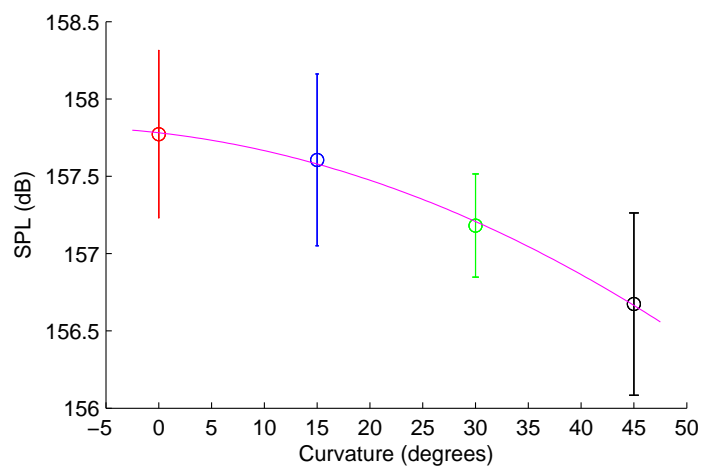


Figure 34: Average SPL with regression analysis.

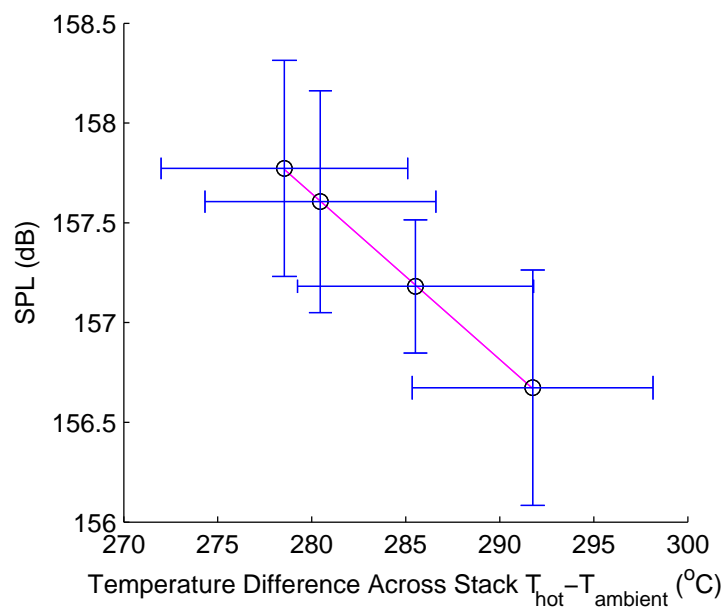


Figure 35: Sound Pressure vs. Temperature Difference

4.0 TRAVELING WAVE INVESTIGATION

The investigation of curvature on the thermoacoustic effect in standing wave engines provided insight into the relationship between the thermal behavior of the stack and the acoustic behavior of the engine. We observed that curvature creates increased losses and quantified the effect of the losses. A logical extension of these findings could then be to apply them to traveling wave thermoacoustic devices. However, there is still a large gap in our understanding of thermal effects in the more complicated geometry of traveling wave devices. Before any sort of future study of the effect of curvature can occur, these thermal effects must first be quantified.

Therefore, the goal of the next component of this study was to examine the thermal behavior of the regenerator in a looped tube traveling wave thermoacoustic engine. The established thermal patterns were then examined for various placements of the regenerator inside the looped tube device to observe the effect of placement on the intensity of the thermoacoustic effect.

4.1 DESIGN AND CONSTRUCTION

4.1.1 Resonator

A looped tube design was chosen for this investigation. Previous investigations have been conducted on the looped tube design by Ceperley et al. [47] and Yazaki et al. [38], with Yazaki's group identifying large viscous losses, suggesting an increase in acoustic impedance. Swift et al. [36] modified the design by adding a resonator to the loop, creating a torus

type engine. This, however, created a secondary system for losses that were later shown by Hu et al. [48] to significantly decrease the efficiency, compared to what had previously been reported. Backhaus et al. [49] have demonstrated that a looped tube engine can be used in tandem with an electric generator, achieving a thermal to electric efficiency of 18%. It can thus be observed that looped tube engines have the potential for efficient conversion of input heat to electric work as well as refrigeration.

A total length of 92in was implemented as a design parameter, leading to an operating frequency of 146Hz in the first mode, with air as the working fluid at atmospheric pressure. The loop-tube was designed using 2 inch nominal diameter schedule 40 PVC and steel pipe, with the heating element positioned in the steel portion of the device, to prevent melting of the PVC. The heating element was designed to have the same nominal resistance as the element in the standing wave design. The straight portions of the pipe were approximately 34 inches long, with the turns approximately 12 inches in length. Standard 90° elbows were joined to the PVC pipe using PVC cement to create the 180° turns required for the loop. The PVC portion of the loop-tube was joined to the steel portion using 4-bolt flanges, with air tightness assured using full-face gaskets. A picture of the device can be seen in Figure 36 with a close up on the steel portion containing the stack shown in Figure 37.

4.1.2 Regenerator

As was discussed above, standing wave and traveling wave engines operate under similar cycles. Several key differences, however, allow traveling wave engines to inherently operate more efficiently than standing wave engines. One such difference lies in the design of the regenerator. Stacks in standing wave engines require the hydraulic diameter to be larger than the thermal penetration depth. Regenerators in traveling wave engines, on the other hand, require a smaller hydraulic diameter to facilitate reversible heat transfer between the medium and the regenerator. Stacked wire meshes have previously been implemented as a regenerator design [36]. However, as discussed above, Zink et al. [32] have found that higher conductivity materials cause secondary losses by carrying heat via conduction. A

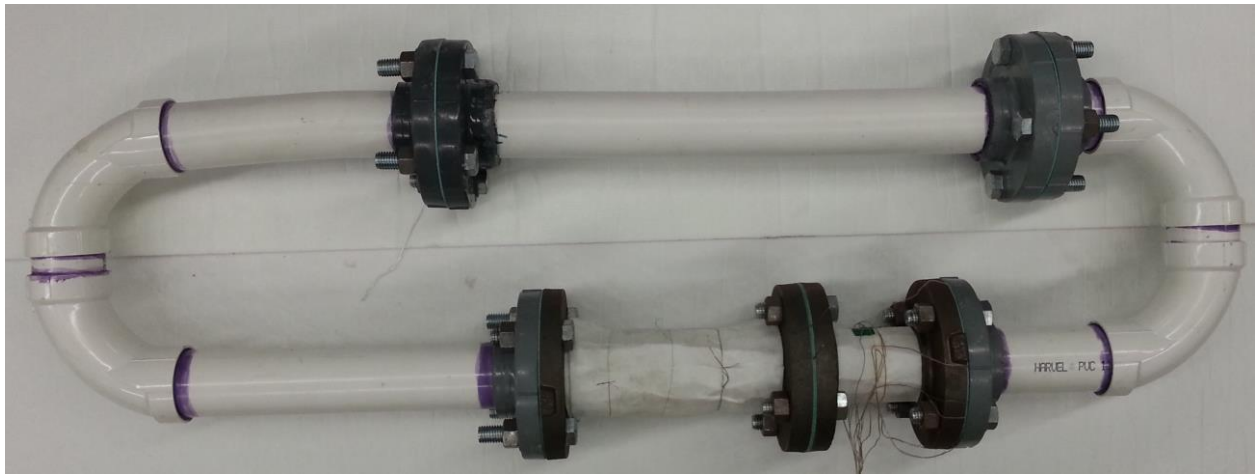


Figure 36: Picture of traveling wave TAE



Figure 37: Housing design used to insure air tightness.



Figure 38: Regenerator used in the construction of the TAE.

square channel ceramic porous material was thus implemented. A pore size of 1.092mm was chosen, providing a ratio of 0.89 between the hydraulic diameter and the thermal penetration depth.

The regenerator, seen in Figure 38, was made using a porous ceramic material (found in catalytic converters in automobile mufflers) with a hole density of approximately 20 holes per inch. The stack was machined to fit into the pipe, and cut to approximately 3.5 inches in length. It was then modified to include an electric heating coil on one side. The heating portion of the coil was designed using 22AWG wire with the lead wires built using 18AWG wire to minimize heat dissipation through wire not directly in contact with the stack.

4.2 EXPERIMENTAL SETUP

Eight K-type thermocouples were used to record the hot and ambient side behavior of the stack. Four of the thermocouples were used to measure the hot side behavior and were mounted in the same position as in the standing wave engine design (see Figure 23). Each was embedded approximately $1/16$ inch from the surface of the hot side and the coil to help achieve a more uniform temperature reading. This would prevent major changes in the recorded temperature if the heated coil changed position due to expansion from heating. Ambient side thermocouples were positioned approximately $1/16$ inch from the center of the stack and mounted at $1/8$, $1/4$, $3/8$, and $1/2$ inches from the surface of the ambient side, shown in Figure 39, to help better evaluate the temperature behavior of the stack.

Data was recorded using a several step voltage increase, starting with a base value at room temperature recorded for 60 seconds to identify any irregularities present in either the testing equipment or the experimental setup. For a four minute period, following the initial baseline recording, a 5V voltage drop was applied across the heating coil. This was followed by three sequential five minute periods of heating at 10V, 15V, and 20V, respectively. After twenty minutes of recording, the current was disconnected and a five minute cool down was recorded. Preliminary data was collected with the ambient side of the stack mounted at 8.5 inches from the edge of the turn of the loop-tube. Following the initial data collection

to validate the testing setup, the stack was moved to the 8.875, 7.25, 6.25, and 5.25 inch positions, as shown in Figure 40. At each position, two separate trials were recorded, one of the performance with oscillation present, the other without the presence of oscillation.

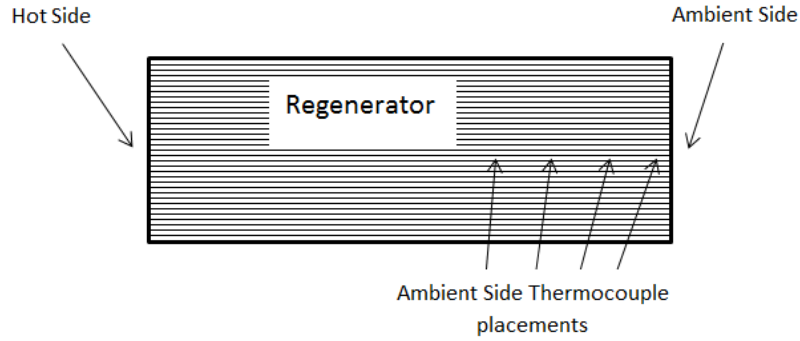


Figure 39: Ambient side thermocouple positioning

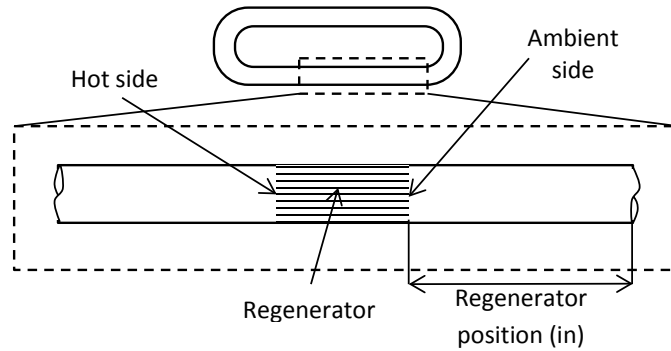


Figure 40: Regenerator position diagram

4.3 RESULTS: STACK POSITIONING EFFECTS ON THERMOACOUSTIC BEHAVIOR

4.3.1 Patterns In Thermoacoustic Behavior

Preliminary data were collected to study the behavior of the individual thermocouples in relation to the presence and the lack of oscillation. Figures 41 and 42 show the behavior of the hot and ambient sides, respectively. The maximum temperature difference between the oscillation and no oscillation runs on the hot side was approximately $154^{\circ}C$, while the maximum temperature difference for the ambient side was approximately $27^{\circ}C$. Figures 43 and 44 show the same data, but are color coded to show the behavior of the individual thermocouples on the hot and ambient sides, respectively. While the hot side showed no meaningful trend between the runs, the ambient side produced significant patterns. Without the presence of oscillations, a linear drop in temperature was expected as the distance from the hot coil increased. As seen in Figure 44, the predicted behavior is displayed, proving the validity of the measurement. The presence of oscillations, however, distorts this pattern and it can be observed that the 3/8 inch position thermocouple displayed higher temperatures than the 1/2 inch position. From this, it can be hypothesized that the highest intensity of the thermoacoustic effect took place at this position. This behavior was also observed in the tests that followed the initial data collection.

It was important to quantify any error that occurred in the acquired measurements. Due to the uneven heating of the coil, an analysis of the variation in the recordings of the hot side thermocouples was crucial to identify the level of variation that was present. Figure 45 shows the temperature difference between runs with oscillations present and oscillations inhibited for the individual thermocouples. Figure 46 shows the variation in the measured temperature difference, reaching a maximum of $18^{\circ}C$, which occurs at the instant the voltage is set to zero from the maximum setting. This temperature variation is normalized against the lower temperature hot side readings, and is shown in Figure 47. The accuracy of the thermocouples was $2.2^{\circ}C$ or 0.75% [50], which through a simple uncertainty analysis provided a level of error of $\approx 18.1^{\circ}C$ (3.09%) to be expected in the recorded measurements.

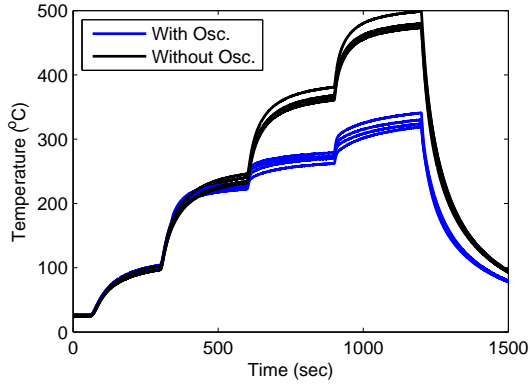


Figure 41: Hot side individual runs.

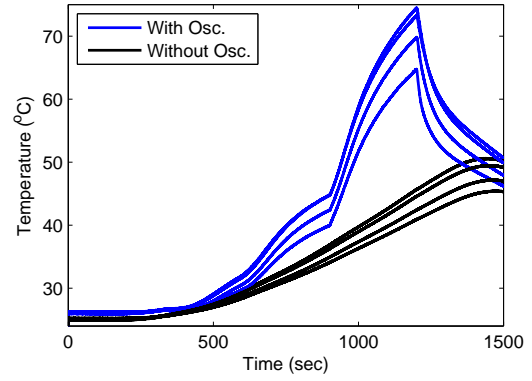


Figure 42: Ambient side individual runs.

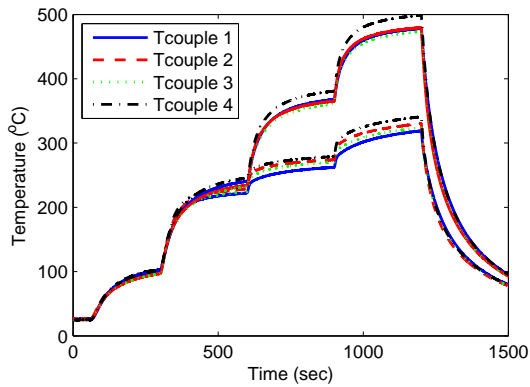


Figure 43: Hot side thermocouple readings.

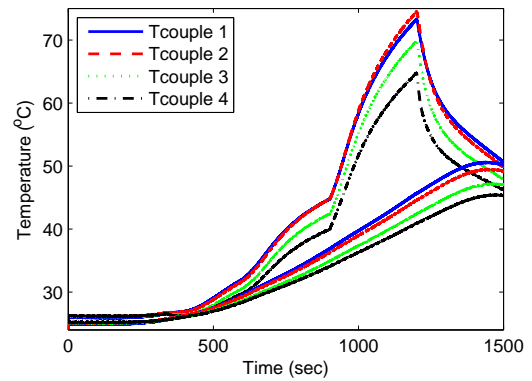


Figure 44: Ambient side thermocouple readings.

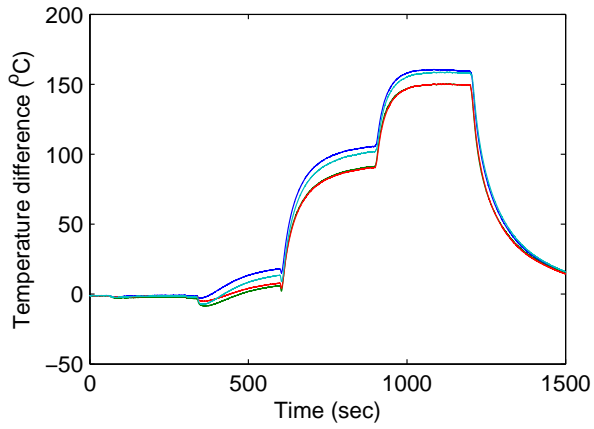


Figure 45: Hot side temperature difference

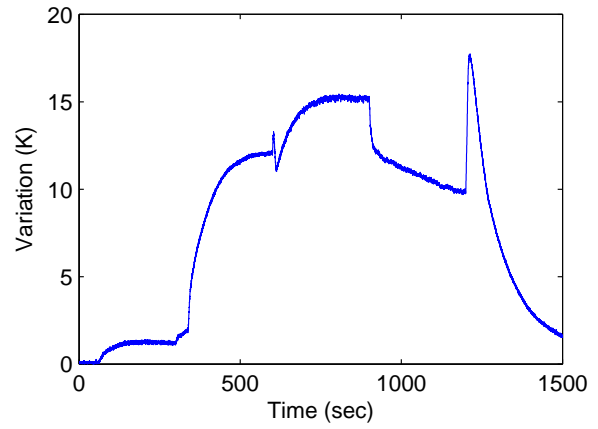


Figure 46: Variation in hot side calculation.

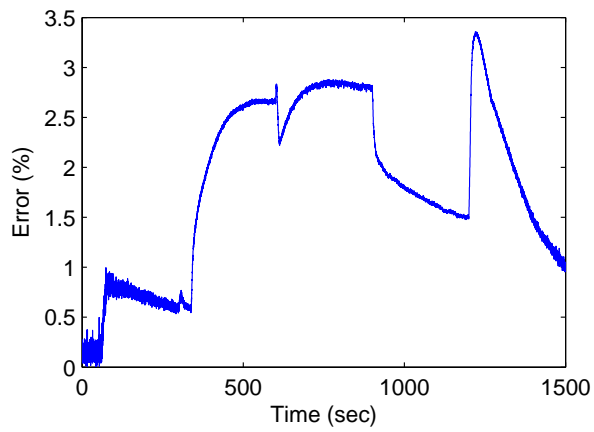


Figure 47: Percent error with respect to lower hot side average

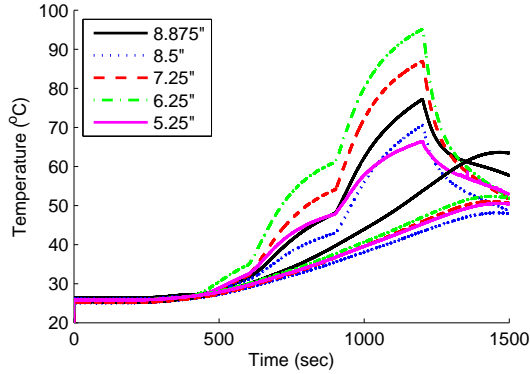


Figure 48: Ambient side averaged oscillation and no oscillation runs.

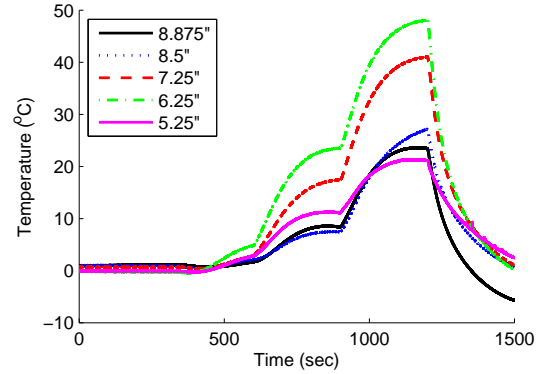


Figure 49: Ambient side temperature difference between run averages.

4.3.2 Ambient Side Behavior

The ambient side showed fairly uniform behavior across the different stack placements, as seen in Figure 48. The runs with oscillations present show a similar pattern of a sharp increase at the points of increase in voltage, that decreases in slope with time. One placement position that shows deviation from the pattern is the 5.25 inch position where the slope seems to decrease at a faster rate than that of the other positions. The no oscillation runs showed slight deviation from a singular pattern, suggesting changing thermal conditions at each stack placement. In order to account for these conditions, Figure 49 shows the temperature differences for each placement between the oscillation and no oscillation runs. The 6.25 inch position shows the largest difference, implying the highest intensity of the thermoacoustic effect.

4.3.3 Hot Side Behavior

The behavior of the hot side showed a significant difference in temperature between runs with oscillation present and runs without oscillation. As predicted, there was a significant drop in temperature when oscillations were introduced. Figure 50 shows the averaged temperatures of the oscillation and no oscillation runs. A tight grouping across the differing placements

can be seen for the oscillation runs and the no oscillation runs. To quantify the effect of the placement of the stack on the thermoacoustic effect on the hot side, the differences between the oscillation and no oscillation readings were taken for each position and are displayed in Figure 51. The 6.25 inch placement shows the largest average temperature difference, in agreement with the ambient side behavior. The 5.25 inch position shows a similarly high temperature difference. However, this high difference in temperature does not correspond to a high temperature difference on the ambient side. It can also be seen in Figure 50 that the oscillation run for that position appears to be outside of the general grouping of the other positions, while the no oscillation run for that same position shows unusual behavior during the 20V period. From this, it can be concluded that an unpredicted variable influenced the hot side readings for that particular position. Increase in contact due to thermal expansion is believed to have affected thermal resistance behavior, artificially reducing the temperature readings.

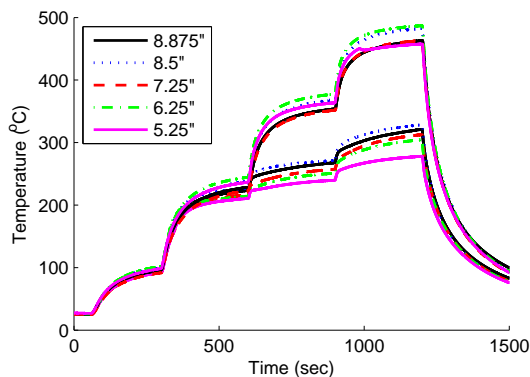


Figure 50: Hot side averaged oscillation and no oscillation runs.

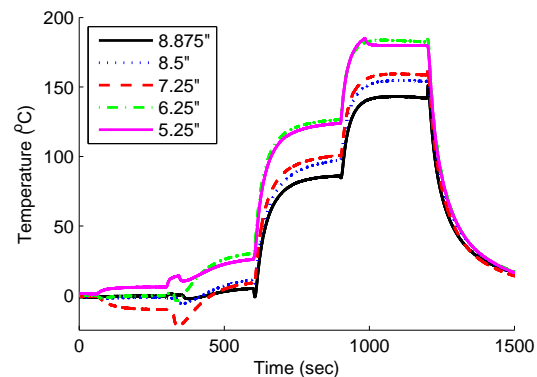


Figure 51: Hot side temperature difference between run averages.

4.3.4 Stack Placement and Intensity of The Thermoacoustic Effect

To help evaluate the intensity of the thermoacoustic effect, the temperature differences for both the ambient and the hot sides were normalized to the highest difference at the 6.25 inch position and are displayed in Figures 52 and 53, respectively. The hot side shows that

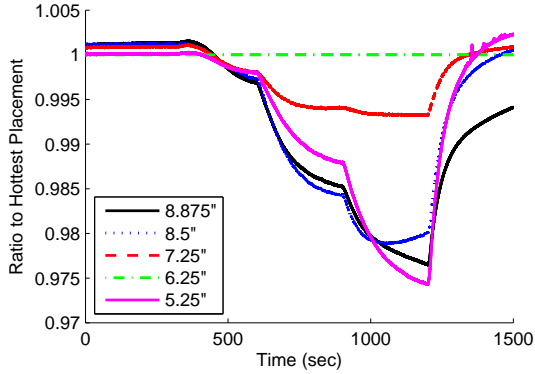


Figure 52: Normalized ambient temperature difference.

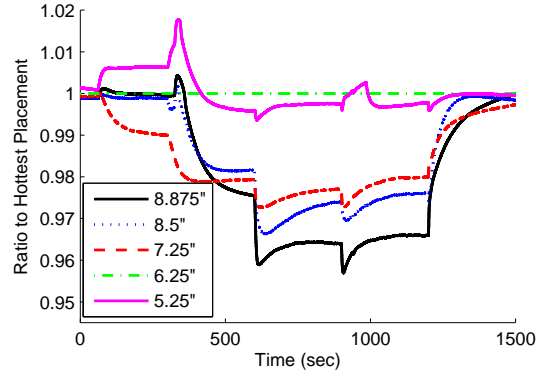


Figure 53: Normalized hot temperature difference.

during the 15V and 20V periods, the ratio between the highest temperature difference and each position stays relatively equal. Sharp decreases in the temperature ratio can also be seen at the times when voltage changes occur, implying the more intense presence of the thermoacoustic effect for the 6.25 inch position. The onset of the thermoacoustic effect can also be observed at approximately 400 seconds, marked by sudden sharp changes in the ratio behavior. The ambient side behavior does not show a linear ratio at each voltage, with only the 7.25 inch position appearing relatively linear for the 15V and 20V time periods. The intensity of the thermoacoustic effect can be observed to increase substantially for the 6.25 inch position with increases in voltage, when compared to other stack positions.

To better quantify the relationship between stack positioning and the intensity of the thermoacoustic effect, surface plots were used to relate the positioning and time to the observed temperature difference, as shown in Figures 54 and 55. For the hot side, a gradual increase in the average temperature difference can be seen in the behavior across all voltages as the stack is moved closer to the edge. A peak appears to occur close to the 0.18 distance ratio to edge after which a mild decrease can be observed. The ambient side behavior shows a substantially better defined pattern of gradual increase with the decrease of the distance to the edge. The 20V averages show the clearest presence of a peak at the same position as

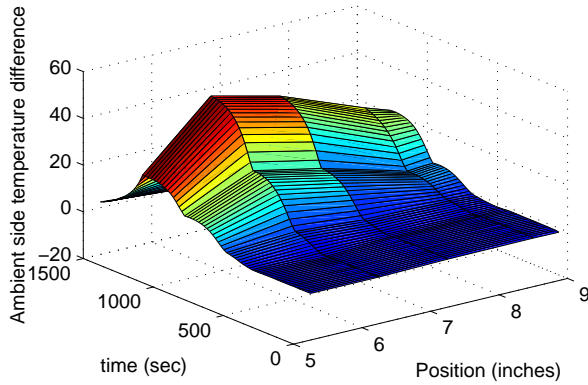


Figure 54: Ambient side stack temperature vs. stack positioning.

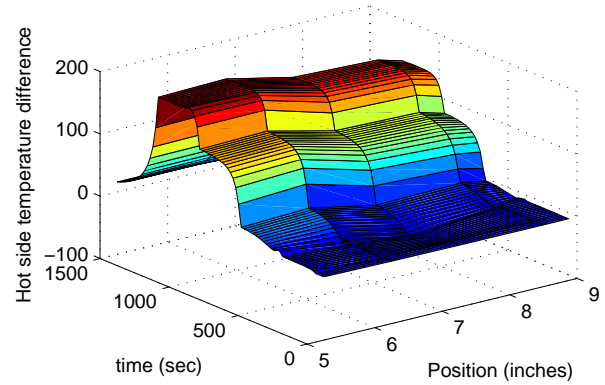


Figure 55: Hot side stack temperature vs. stack positioning.

the hot side. However, the subsequent drop is far more significant for the ambient side than the hot side. Both figures match on a peak close to the 0.18 distance ratio and show that positioning has a significant impact on the intensity of the thermoacoustic effect, and thus the efficiency of the TAE.

4.4 DISCUSSION

The investigation on the standing wave thermoacoustic engine has shown a strong correlation between the temperature difference across the stack and the acoustic power. This concept can be implemented in this investigation by combining the hot and ambient temperature differences to demonstrate a total difference provided by the thermoacoustic effect. Figure 56 shows the total temperature difference across the regenerator with respect to time for each position. Figure 57 shows a three-dimensional surface plot relating both the time and position to the total temperature difference. A pronounced peak emerges for the 0.18 position of the regenerator, as previously observed in the individual temperature difference evaluations.

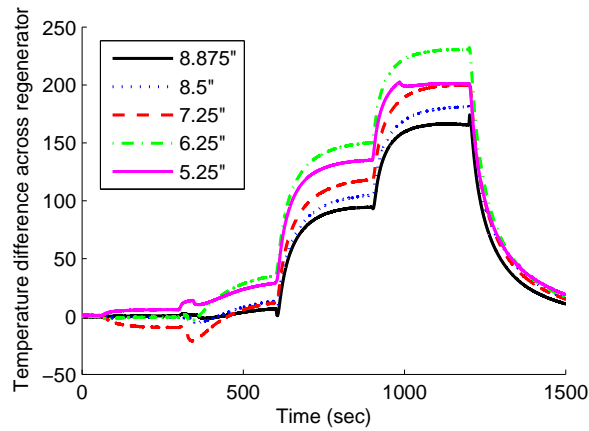


Figure 56: Temperature difference across regenerator

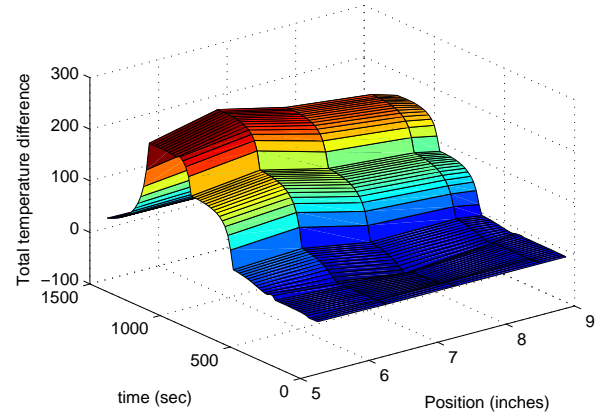


Figure 57: Hot side stack temperature vs. stack positioning.

While it is yet unclear as to the cause of the effect of stack positioning, it is suggested that an investigation in the loss mechanisms in a looped tube type engine be conducted. A focus on Rayleigh streaming interaction with the curvature of the loop and acoustic losses caused by the curvature may lead to new improvements of the looped tube engine.

5.0 CONCLUSIONS AND FURTHER RECOMMENDATIONS

5.1 CONCLUSIONS

We have analyzed the temperature and acoustic behavior of a standing wave thermoacoustic engine and the way that this behavior changes as the curvature of the resonator of the engine is changed from an initial 0° to a final 45° position in four increments. By recording the performance of the engine three times for a period of 5 minutes each, at each curvature, we were able to acquire reliable average values for the hot and ambient side temperatures of the engine as well as similarly reliable values for the sound pressure level. Using this data, we were able to acquire overall average values that presented a very strong positive linear relationship between hot side stack temperature and curvature. The SPL averages produced a very strong negative quadratic relationship between curvature and SPL, with the peak of the quadratic function close to the 0° position. The ambient side behavior did not produce any meaningful relationship over all four curvatures. However, a fairly strong negative relationship could be deduced, when the 0° curvature is excluded from the analysis. The overall data agrees with the CFD predictions given in [31, 51]. The results described above prove that it is feasible to design thermoacoustic devices with curved resonators. This could allow for the footprint of the devices to be reduced without causing a significant drop in performance, making their implementation easier when faced with limited space. A possible use for these findings is for TARs on mobile platforms, such as vehicles that run on or transport supercooled fluids.

The standing wave engine investigation was followed by an investigation of a traveling wave engine. We investigated a looped tube design TAE and have shown the impact of stack positioning inside the looped tube on its efficiency. Using the temperature difference

between oscillation and no oscillation runs for each stack position, the effect was measured for the hot and ambient sides of the stack. A significant increase in efficiency can be seen when the stack is moved to approximately 0.18 of the total straight length from the edge, measured from the ambient side facing the edge. More effective conversion of thermal energy to thermoacoustic energy increases the amount of cooling produced by a given amount of heat and thus increases the COP. Increases in the COP of TAEs can help make it more competitive with the traditional VCR, broadening the range of industries for its use.

5.2 FUTURE WORK

In the effort to continue improving the performance of TAEs and TARs, further investigation into loss mechanisms is required. As stated above, thermal losses have not received a large amount of attention and have been shown to be a significant contributor to reducing the overall efficiency of thermoacoustic devices. Viscous losses in the heat exchangers have also been shown to significantly impact their performance. Thus, a deeper investigation into decreasing viscous dissipation and increasing heat transfer to the regenerator has significant potential. Possible methods for experimentally quantifying viscous dissipation could include the comparison of SPL to the temperature variation across the stack for various exchanger designs. Numerical simulations of traveling wave behavior around the stack could additionally help identify regions of high viscous and thermal dissipation.

BIBLIOGRAPHY

- [1] A. Putnam, W. R. Dennis, *Survey of organ-pipe oscillations in combustion systems*, The Journal of the Acoustical Society of America, **Vol. 28** pp. 246–259 (1956).
- [2] B. Higgins, *Nicholson's Journal* p. 130 (1802).
- [3] P. L. Rijke, *Notiz ber eine neue Art, die in einer an beiden enden offenen Rhre enthaltene Luft in Schwingungen zu versetzen*, Annals of Physics, **Vol. 107** pp. 339–34 (1859).
- [4] C. Sondhauss, *Ueber die Schallschwingungen der Luft in erhitzten Glasrhren und in gedeckten Pfeifen von ungleicher Weite*, Annals of Physics and Chemistry, **Vol. 79** pp. 1–34 (1850).
- [5] G. Kirchoff, *Ueber den Einfluss der Wrmeleitung in einem Gase auf die Schallbewegung*, Annals of Physics, **Vol. 134** pp. 177–193 (1868).
- [6] H. Kramers, *Vibrations of a gas column*, Physica, **Vol. 15** pp. 971–984 (1949).
- [7] N. Rott, *Damped and thermally driven acoustic oscillations in wide and narrow tubes*, Zeitschrift fr angewandte Mathematik und Physik, **Vol. 20** pp. 230–243 (1969).
- [8] P. H. Ceperley, *Gain and efficiency of a short traveling wave heat engine*, Journal of the Acoustical Society of America, **Vol. 77** pp. 1239–1244 (1985).
- [9] T. Yazaki, A. Iwata, T. Maekawa, A. Tominaga, *Traveling Wave Thermoacoustic Engine in a Looped Tube*, Physical Review Letters, **Vol. 81 (15)** pp. 3128–3131 (1998).
- [10] G. W. Swift, S. Backhaus, *A resonant, self-pumped, circulating thermoacoustic heat exchanger*, Journal of the Acoustical Society of America, **Vol. 16 (5)** pp. 2923–2938 (2004).
- [11] K. I. Matveev, C. D. Richards, N. Shafie-Tehrany, *Small-scale Thermoacoustic Engine Demonstrator*, Proceedings of Power MEMS (2008).
- [12] G. W. Swift, *Thermoacoustic Engines*, Journal of the Acoustical Society of America, **Vol. 84 (4)** pp. 1145–1180 (1988).

- [13] G. W. Swift, *Thermoacoustics: A unifying perspective for some engines and refrigerators*, Acoustical Society of America, Melville NY (2002).
- [14] S. Backhaus, G. W. Swift, *A thermoacoustic Stirling heat engine: Detailed Study*, Journal of the Acoustical Society of America, **Vol. 107 (6)** pp. 3148–66 (2000).
- [15] S. Backhaus, G. Swift, R. Reid, *High-temperature self-circulating thermoacoustic heat exchanger*, Applied Physics Letters, **Vol. 87** p. 014102 (2005).
- [16] Y. Ueda, T. Biwa, U. Mizutani, T. Yazaki, *Experimental studies of a thermoacoustic Stirling prime mover and its application to a cooler*, Journal of the Acoustical Society of America, **Vol. 72 (3)** pp. 1134–1141 (2003).
- [17] C. M. DeBlok, N. A. Hendrikus, J. V. Rijt, *US Patent 6314740* (2001).
- [18] Z. Yu, A. Jaworski, *Impact of acoustic impedance and flow resistance on the power output capacity of the regenerators in travelling-wave thermoacoustic engines.*, Energy Conversion and Management, **Vol. 51** pp. 350–359 (2010).
- [19] S. Q. Abu-Ein, S. M. Fayyad, W. Momani, M. Al-Bousoul, *Performance analysis of solar powered absorption refrigeration system*, Heat and Mass Transfer pp. 137–145 (2009).
- [20] T. Jin, G. B. Chen, B. R. Wang, S. Y. Zhang, *Application of thermoacoustic effect to refrigeration*, Review of Scientific Instruments, **Vol. 74 (3)** pp. 677–679 (2003).
- [21] S. Vanapalli, M. Lewis, Z. Gan, R. Radebaugh, *120 Hz pulse tube cryocooler for fast cooldown to 50 K*, Applied Physics Letter, **Vol. 90** (2007).
- [22] P. E. Phelan, J. Swanson, F. Chiriac, V. Chiriac, *Designing a mesoscale vapor-compression refrigerator for cooling high-power microelectronics*, Thermal and Thermomechanical Phenomena in Electronic Systems (ITHERM'04) (2004).
- [23] C. Herman, Z. Travnicek, *Cool Sound: The future of refrigeration? Thermodynamic and heat transfer issues in thermoacoustic refrigeration*, Heat and Mass Transfer, **Vol. 42** pp. 492–500 (2006).
- [24] M. E. H. Tijani, J. C. H. Zeegers, A. T. A. M. de Waele, *The optimal stack spacing for thermoacoustic refrigeration*, The Journal of the Acoustical Society of America, **Vol. 112** pp. 128–133 (2002).
- [25] H. Babaei, K. Siddiqui, *Design and optimization of thermoacoustic devices*, Energy Conversion and Management, **Vol. 49** pp. 3585–3598 (2008).
- [26] J. R. Olson, G. W. Swift, *Energy Dissipation In Oscillating Flow Through Straight And Coiled Pipes*, The Journal of the Acoustical Society of America, **Vol. 100** pp. 2123–2131 (1996).

- [27] N. Rott, *Damped and thermally driven acoustic oscillations in wide and narrow tubes*, *Zeitschrift für angewandte Mathematik und Physik*, **Vol. 20** pp. 230–243 (1969).
- [28] W. P. Arnott, H. E. Bass, R. Raspet, *General formulation of thermoacoustics for stacks having arbitrarily shaped pore cross sections*, *Journal of the Acoustical Society of America*, **Vol. 60 (6)** pp. 3228–3237 (1991).
- [29] M. E. H. Tijani, J. C. H. Zeegers, A. T. A. M. de Waele, *Design of thermoacoustic refrigerators*, *Cryogenics*, **Vol. 42** pp. 49–57 (2002).
- [30] M. E. H. Tijani, J. C. H. Zeegers, A. T. A. M. de Waele, *The optimal stack spacing for thermoacoustic refrigeration*, *Journal of the Acoustical Society of America*, **Vol. 112 (1)** pp. 126–133 (2002).
- [31] F. Zink, J. S. Vipperman, L. A. Schaefer, *Heat Transfer Analysis in Thermoacoustic Regenerators using CFD Simulation*, in *Proceedings of the ASME Summer Heat Transfer Conference* (2009).
- [32] F. Zink, J. S. Vipperman, L. A. Schaefer, *Influence of the thermal properties of the driving components on the performance of a thermoacoustic engine*, in *Proceedings of the International Mechanical Engineering Congress and Exhibition (IMECE)* (2009).
- [33] J. R. Olson, G. Swift, *Acoustic Streaming in pulse tube refrigerators: Tapered Pulse Tubes*, *Cryogenics*, **Vol. 37 (12)** pp. 769–776 (1997).
- [34] V. Gusev, S. Job, H. Bailliet, P. Lotton, M. Bruneau, *Acoustic streaming in annular thermoacoustic prime-movers*, *Journal of the Acoustical Society of America*, **Vol. 108 (3)** pp. 934–945 (2000).
- [35] G. Penelet, V. Gusev, P. Lottona, M. Bruneau, *Nontrivial influence of acoustic streaming on the efficiency of annular thermoacoustic prime movers*, *Physics Letters A*, **Vol. 351** pp. 268–273 (2006).
- [36] G. Swift, D. L. Gardner, S. Backhaus, *Acoustic Recovery of lost power in pulse tube refrigerators*, *Journal of the Acoustical Society of America*, **Vol. 105 (2)** pp. 711–724 (1998).
- [37] D. F. Gaitan, A. Gopinath, A. A. Atchley, *Experimental study of acoustic turbulence and streaming in a thermoacoustic stack*, *Journal of the Acoustical Society of America*, **Vol. 96** p. 3220 (1994).
- [38] T. Yazaki, A. Tominaga, *Measurement of sound generation in thermoacoustic oscillations*, in *Proceedings of the Royal Society - Mathematical, Physical and Engineering Sciences (Series A)* (1998).
- [39] M. Thompson, A. Atchley, *Simultaneous measurement of acoustic and streaming velocities in a standing wave using laser Doppler anemometry*, *The Journal of the Acoustical Society of America*, **Vol. 117** p. 1828 (2005).

- [40] A. A. Atchley, H. E. Bass, T. J. Hoffer, H.-T. Lin, *Study of a thermoacoustic prime mover below onset of self-oscillation*, Journal of the Acoustical Society of America, **Vol. 91 (2)** pp. 734–743 (1992).
- [41] A. A. Atchley, *Standing wave analysis of a thermoacoustic prime mover below onset of self-oscillation*, Journal of the Acoustical Society of America, **Vol. 92 (5)** pp. 2907–14 (1992).
- [42] A. Atchley, T. Hoffer, M. Muzzerall, M. Kite, C. Ao, *Acoustically generated temperature gradients in short plates*, The Journal of the Acoustical Society of America, **Vol. 88** p. 251pp (1990).
- [43] A. J. Organ, *The Regenerator and the Stirling Engine*, Mechanical Engineering Publications Limited (1997).
- [44] G. Chen, K. Tang, T. Jin, *Advances in thermoacoustic engine and its application to pulse tube refrigeration*, Chinese Science Bulletin, **Vol. 49 (13)** pp. 1319–1328 (2004).
- [45] D. G. Holmberg, G. S. Chen, H. T. Lin, A. M. Wo, *Thermal modeling and performance analysis of a thermoacoustic refrigerator*, Journal of the Acoustical Society of America, **Vol. 114 (2)** pp. 782–791 (2003).
- [46] F. Zink, H. Waterer, R. Archer, L. Schaefer, *Geometric Optimizing of a Thermoacoustic Regenerator*, International Journal of Thermal Sciences, **Vol. 48 (12)** pp. 2309–2322 (2009).
- [47] P. H. Ceperley, *A pistonless Stirling Engine - The traveling wave heat engine*, Journal of the Acoustical Society of America, **Vol. 66 (5)** pp. 1508–1513 (1979).
- [48] Z. J. Hu, Z. Li, Q. Li, Q. Li, *Evaluation of thermal efficiency and energy conversion of thermoacoustic Stirling engines*, Energy Conversion and Management, **Vol. 51** pp. 802–812 (2010).
- [49] S. Backhaus, *Traveling-wave thermoacoustic electric generator*, Applied Physics Letters, **Vol. 85** pp. 1085–1087 (2004).
- [50] OMEGA, <http://www.omega.com/temperature/Z/pdf/z218-220.pdf>.
- [51] F. Zink, J. S. Viperman, L. A. Schaefer, *CFD Simulation of a Thermoacoustic Engine with Coiled Resonator*, International Communications of Heat and Mass Transfer, **Vol. 30 (3)** pp. 226–229 (2010).